

# The High Redshift Integrated Sachs-Wolfe Effect

Jun-Qing Xia<sup>1,\*</sup>, Matteo Viel<sup>2,3,†</sup>, Carlo Baccigalupi<sup>1,3,‡</sup> and Sabino Matarrese<sup>4,5,§</sup>

<sup>1</sup>*Scuola Internazionale Superiore di Studi Avanzati, Via Beirut 2-4, I-34014 Trieste, Italy*

<sup>2</sup>*INAF-Osservatorio Astronomico di Trieste, Via G.B. Tiepolo 11, I-34131 Trieste, Italy*

<sup>3</sup>*INFN/National Institute for Nuclear Physics, Via Valerio 2, I-34127 Trieste, Italy*

<sup>4</sup>*Dipartimento di Fisica “G. Galilei”, Università di Padova, Via Marzolo 8, I-35131 Padova, Italy and*

<sup>5</sup>*INFN, Sezione di Padova, Via Marzolo 8, I-35131 Padova, Italy*

In this paper we rely on the quasar (QSO) catalog of the Sloan Digital Sky Survey Data Release Six (SDSS DR6) of about one million photometrically selected QSOs to compute the Integrated Sachs-Wolfe (ISW) effect at high redshift, aiming at constraining the behavior of the expansion rate and thus the behaviour of dark energy at those epochs. This unique sample significantly extends previous catalogs to higher redshifts while retaining high efficiency in the selection algorithm. We compute the auto-correlation function (ACF) of QSO number density from which we extract the bias and the stellar contamination. We then calculate the cross-correlation function (CCF) between QSO number density and Cosmic Microwave Background (CMB) temperature fluctuations in different subsamples: at high  $z > 1.5$  and low  $z < 1.5$  redshifts and for two different choices of QSO in a conservative and in a more speculative analysis. We find an overall evidence for a cross-correlation different from zero at the  $2.7\sigma$  level, while this evidence drops to  $1.5\sigma$  at  $z > 1.5$ . We focus on the capabilities of the ISW to constrain the behaviour of the dark energy component at high redshift both in the  $\Lambda$ CDM and Early Dark Energy cosmologies, when the dark energy is substantially unconstrained by observations. At present, the inclusion of the ISW data results in a poor improvement compared to the obtained constraints from other cosmological datasets. We study the capabilities of future high-redshift QSO survey and find that the ISW signal can improve the constraints on the most important cosmological parameters derived from Planck CMB data, including the high redshift dark energy abundance, by a factor  $\sim 1.5$ .

## I. INTRODUCTION

The cosmic microwave background (CMB) measurements of temperature anisotropies and polarization [1] and the redshift-distance measurements of Type Ia Supernovae (SNIa) at  $z < 2$  [2], have established that the universe is undergoing an accelerated phase of expansion and that its total energy budget is dominated by a dark energy component. The nature of this component is still unknown and many observational probes have been proposed to test its properties and redshift evolution either in the standard  $\Lambda$ -Cold Dark Matter ( $\Lambda$ CDM), modified gravity or quintessence models (for a review see Ref. [3]). While the CMB is a powerful cosmological probe of the universe at  $z \sim 1100$ , the anisotropies present in CMB data (kinetic and thermal Sunyaev-Zeldovich effects, weak lensing and the Integrated Sachs-Wolfe effect) contain precious information on the large scale structure that formed at much lower redshift. These effects can be studied and detected by cross-correlating CMB data with tracers of the large scale structure (LSS) such as galaxies or quasars. Here, we will focus on the Integrated Sachs-Wolfe effect [4].

The first investigations of CMB-LSS cross-correlations were made in Refs. [5, 6] using X-ray observations

(HEAO data) and CMB data from the COBE satellite that allowed to constrain the bias of X-ray sources and put upper limits on the amount of a cosmological constant energy density. In a more recent series of works, a similar set of analyses have been carried which relied on CMB data from the WMAP satellite and a variety of LSS probes such as NVSS (NRAO VLA Sky Survey) radio galaxies [7, 8], the Two Micron All Sky Survey (2MASS) [9, 10], galaxies from Sloan Digital Sky Survey (SDSS) DR4 and DR5 [11, 12]. There is overall agreement between the different groups in finding an evidence for a positive ISW signal at the  $\sim 3\sigma$  confidence level. Even more recently, several groups have started to analyze the CMB-LSS correlations in a more comprehensive framework fully exploiting the capabilities of the SDSS (DR5, DR6), addressing the many possible systematic effects involved, modeling the statistical error bars and covariance properties of the data with different methods and combining the different tracers in the using Monte Carlo Markov Chains estimators for deriving the cosmological parameters (e.g. [13, 14, 15, 16]).

Although the results obtained from the CMB-LSS are promising and have provided independent evidences for the presence of a dark energy component, their quantitative use as cosmological probes is still to be fully exploited. The timely convergence of future LSS surveys like SDSS-III [17, 18] and high resolution CMB experiment like Planck<sup>1</sup> will offer the opportunity to fur-

---

\*Electronic address: xia@sissa.it

†Electronic address: viel@oats.inaf.it

‡Electronic address: bacci@sissa.it

§Electronic address: sabino.matarrese@pd.infn.it

---

<sup>1</sup> Available at <http://www.rssd.esa.int/planck/>.

ther explore the valuable information of the ISW and in general of several other LSS-CMB cross-correlations in a quantitative way (e.g. [19]). Present efforts are particularly concentrated on quantifying several systematic effects that are possibly affecting the ISW signal such as noise by local variance [20], redshift space distortions [21], non-linear contributions [22], uncertainties in the bias estimates [23] and contributions due to voids and clusters to the overall ISW signal [24].

However, once the systematic effects will be under control the ISW is likely to become a powerful cosmological probe able to constrain for example the contribution of massive neutrinos [25] or evolution of the dark energy component at high redshift (e.g. [26]), which is poorly constrained by observations at the present [27]. In this paper we focus on this latter issue and push the ISW capabilities to the highest possible redshift regime in a way similar to that used by Ref. [13], using the recently released SDSS DR6-QSO catalog of about one million photometrically selected QSOs in order to give constraints on some dark energy models.

Among all the dynamical dark energy models, we will consider early dark energy (EDE) ones, in which a small fraction of dark energy is present up to the last scattering surface (lss), unlike  $\Lambda$ CDM for which  $\Omega_{\text{DE}}(z_{\text{lss}}) \simeq 0$ . The differences between early dark energy models and pure  $\Lambda$ CDM are particularly evident at high redshifts, over a large fraction of the cosmic time, when the first structures form. EDE has been shown to influence the growth of cosmic structures (both in the linear and in the non-linear regime), to change the age of the universe, to have an influence on CMB physics, to impact on the reionization history of the universe, to modify the statistics of giant arcs in strong cluster lensing statistics (e.g. [28, 29, 30, 31, 32, 33, 34, 35, 36, 37, 38, 39, 40]). Recently some EDE models have been investigated by Refs. [41, 42], focussing in particular on using present and future weak lensing observables and measurements of the growth factors of density perturbations obtained via Lyman- $\alpha$  forest observations.

The structure of the paper is as follows: in Sec. II and Sec. III we briefly review the theoretical background of the ISW effect and describe the quasar catalog used, respectively. Sec. IV and Sec. V contain the analysis of ACF of QSO number density and CCF between QSO number density and CMB temperature fluctuations. In Sec. VI we present the theoretical framework of the early dark energy model and the datasets we used. Sec. VII contains the bulk of our results, while Sec. VIII is dedicated to forecasting with future datasets. We conclude with a discussion in Sec. IX.

## II. ISW EFFECT

In this section we briefly review the basics of ISW effect focussing on its cross-correlation with the number density of astrophysical sources (e.g. Refs. [9, 43, 44]).

The temperature anisotropy due to the ISW effect is expressed as an integral of the time derivative of the gravitational potential  $\Phi$  over conformal time  $\eta$

$$\frac{\Delta T}{T}^{\text{ISW}}(\hat{\mathbf{n}}) = -2 \int \dot{\Phi}[\eta, \hat{\mathbf{n}}(\eta_0 - \eta)] d\eta. \quad (1)$$

For scales within the horizon, we can relate the gravitational potential  $\Phi$  to the comoving density field  $\delta$  by Poisson equation:

$$\begin{aligned} \nabla^2 \Phi(x) &= \frac{4\pi G \rho_m}{a} \delta_m(x) \quad \Rightarrow \\ \Phi(\mathbf{k}, z) &= -\frac{3H_0^2}{2c^2} \Omega_m (1+z) \frac{\delta_m(\mathbf{k}, z)}{k^2}, \end{aligned} \quad (2)$$

where  $\Omega_m$  is the ratio of the matter density to the critical density today,  $H_0$  is the Hubble constant today,  $c$  is the speed of light,  $z$  is the redshift, and  $k$  is the comoving wave number. From Eqs. (1,2) one can appreciate that when a CMB photon falls into a gravitational potential well, it gains energy, while it loses energy when it climbs out of a potential well. These effects exactly cancel if the potential is time independent, such as the matter dominated era ( $\delta_m \sim a$ ) in which the gravitational potential stays constant,  $\dot{\Phi} = 0$  and no ISW is produced. However, when dark energy or curvature become important at later times, the potential evolves as the photon passes through it. In this case,  $\dot{\Phi} \neq 0$  and additional CMB anisotropies will be produced.

The ISW effect of interest here is the one produced at relatively late time, when the dark energy component is dominating the universe density budget, causing a change in the time dependence of the expansion rate, departing from pure matter dominance, and a consequent time evolution of the gravitational potentials. An early ISW, not considered here, is injected soon after decoupling, when the expansion rate time dependence is in the transition between radiation and matter dominance. Observing the late-time ISW can be a powerful way of probing dark energy and its evolution. However, the most significant ISW effect contributes to the CMB anisotropies on large scales that are strongly affected by the cosmic variance. Fortunately, this problem can be solved by the cross-correlation between ISW temperature fluctuation and the density of astrophysical objects like galaxies or quasars (in the following calculations we will use the quasar catalog). The observed quasar (QSO) density contrast in a given direction  $\hat{\mathbf{n}}_1$  will be:

$$\begin{aligned} \delta_q(\hat{\mathbf{n}}_1) &= \int f(z) \delta_m(\hat{\mathbf{n}}_1, z) dz \\ &= \int b_q(z) \frac{dN}{dz}(z) \delta_m(\hat{\mathbf{n}}_1, z) dz, \end{aligned} \quad (3)$$

where  $b_q(z)$  is an assumed scale-independent bias factor relating the quasar overdensity to the mass overdensity,  $\delta_q = b_q \delta_m$ ,  $dN/dz$  is the normalized selection function of the survey. Since the density  $\delta_m$  is related to the gravitational potential  $\Phi$ , the observed galaxy density will

be correlated with the ISW temperature in the nearby direction  $\hat{\mathbf{n}}_2$ :

$$\frac{\Delta T}{T}(\hat{\mathbf{n}}_2) = -2 \int \frac{d\Phi}{dz}(\hat{\mathbf{n}}_2, z) dz . \quad (4)$$

Given a map of CMB and QSO survey, the angular auto-correlation and cross-correlation functions can be easily expressed in the harmonic space:

$$\begin{aligned} C^{\text{qT}}(\theta) &\equiv \left\langle \frac{\Delta T}{T}(\hat{\mathbf{n}}_1) \delta_{\text{q}}(\hat{\mathbf{n}}_2) \right\rangle \\ &= \sum_{l=2}^{\infty} \frac{2l+1}{4\pi} C_l^{\text{qT}} P_l[\cos(\theta)] , \end{aligned} \quad (5)$$

$$\begin{aligned} C^{\text{qq}}(\theta) &\equiv \langle \delta_{\text{q}}(\hat{\mathbf{n}}_1) \delta_{\text{q}}(\hat{\mathbf{n}}_2) \rangle \\ &= \sum_{l=2}^{\infty} \frac{2l+1}{4\pi} C_l^{\text{qq}} P_l[\cos(\theta)] , \end{aligned} \quad (6)$$

where  $\theta = |\hat{\mathbf{n}}_1 - \hat{\mathbf{n}}_2|$  and the auto-correlation and cross-correlation power spectra are given by:

$$C_l^{\text{qT}} = \frac{2}{\pi} \int k^2 dk P(k) I_l^{\text{ISW}}(k) I_l^{\text{q}}(k) , \quad (7)$$

$$C_l^{\text{qq}} = \frac{2}{\pi} \int k^2 dk P(k) [I_l^{\text{q}}(k)]^2 , \quad (8)$$

where  $P(k)$  is the matter power spectrum today and the functions  $I_l^{\text{ISW}}(k)$  and  $I_l^{\text{q}}(k)$  are:

$$I_l^{\text{ISW}}(k) = -2 \int \frac{d\Phi(k)}{dz} j_l[k\chi(z)] dz , \quad (9)$$

$$I_l^{\text{q}}(k) = \int b_{\text{q}}(z) \frac{dN}{dz}(z) \delta_{\text{m}}(k, z) j_l[k\chi(z)] dz , \quad (10)$$

where  $j_l(x)$  are the spherical Bessel functions, and  $\chi$  is the comoving distance. In the following, we use the public package `CAMB_sources`<sup>2</sup> to calculate the theoretical angular auto-correlation and cross-correlation functions.

### III. QUASAR CATALOG

We use the SDSS DR6 quasar catalog released by Ref. [45] (hereafter DR6-QSO). This unique quasar catalog contains about  $N_{\text{q1}} \approx 10^6$  objects with photometric redshifts between 0.065 and 6.075, covering almost all of the northern hemisphere of the galaxy plus three narrow stripes in the southern, for a total area of 8417 deg<sup>2</sup> ( $\sim 20\%$  area of the whole sky). Photometrically selected QSOs have become particularly important in the last few years due to the higher selection efficiency reached, that has enabled their use for meaningful statistical/cosmological analysis. The DR6-QSO data set

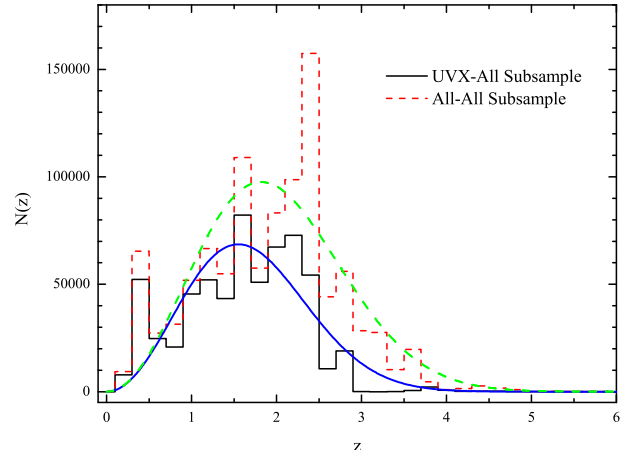


FIG. 1: Redshift distributions of the two quasar subsamples: black solid line is for the “UVX-All” subsample while red dashed line is for the “All-All” subsample. We also plot the theoretical redshift distribution function  $dN/dz$  of two subsamples: blue solid line and green dashed line are for “UVX-All” and “All-All” subsample, respectively.

extends previous similar SDSS data sets with  $\sim 95\%$  efficiency [46, 47]. The main differences are due to the fact that DR6-QSO probes QSOs at higher redshift and also contains putative QSOs flagged as to have ultra violet excess (UVX objects). We refer the reader to Ref. [45] for a very detailed description of the object selection with the non-parametric Bayesian classification kernel density estimator (NBC-KDE) algorithm.

For our purposes we rely on the electronically published table that contains only objects with the “good” flag with values within the range [0, 6], and we label this as “All-All” subsample. The higher the value, the more probable for the object to be a real QSO (see Section 4.2 of Ref. [45] for details). As a further more conservative criterion, we will present results for a subset with “uvxts=1”, i.e. objects clearly showing a UV excess which should be a signature of a QSO spectrum. We are left with  $N_{\text{q2}} \approx 6 \times 10^5$  quasars and we refer to this sample as “UVX-All” subsample. This second choice is clearly more conservative than the first one and thereby results should be trusted more at a quantitative level.

For simplicity, we assume that the redshift distribution  $dN/dz$  of the DR6-QSO sample is approximated by the function:

$$\frac{dN}{dz}(z) = \frac{\beta}{\Gamma(\frac{m+1}{\beta})} \frac{z^m}{z_0^{m+1}} \exp \left[ - \left( \frac{z}{z_0} \right)^\beta \right] , \quad (11)$$

where  $m$ ,  $\beta$  and  $z_0$  are three free parameters, which are dependent on the redshift distribution of quasar number density. For the “All-All” subsample, we find that  $m = 2.00$ ,  $\beta = 2.20$ , and  $z_0 = 1.90$ . The mean redshift of this

<sup>2</sup> Available at <http://camb.info/sources/>.

subsample is  $\bar{z} \sim 1.80$ . The “UVX-All” subsample has  $m = 2.00$ ,  $\beta = 2.20$ ,  $z_0 = 1.62$  and its mean redshift is  $\bar{z} \sim 1.49$ . The distributions are shown together with the redshift distribution of the quasar number density in Fig. 1. In this plot we do not normalize the distributions to be unity.

Furthermore, we also take into account the magnification bias effect which could be important for the SDSS QSOs. In the presence of magnification bias, the relevant quantity entering Eq. (10) is the function  $f(z)$  given by [15]:

$$f(z) = b(z) \frac{dN}{dz}(z) + \int_z^\infty W(z, z') [\alpha(z') - 1] \frac{dN}{dz'} dz', \quad (12)$$

where  $\alpha(z')$  is the slope of the number counts of the quasar number density as a function of flux:  $N(> F) \propto F^{-\alpha}$ . For simplicity, in our analysis we set  $\alpha \equiv 0.9$  in the whole redshift region. Here in the flat universe the lensing window function  $W(z, z')$  is [15]:

$$W(z, z') = \frac{3}{2} \Omega_m H_0^2 \frac{1+z}{cH(z)} \chi^2(z) \left[ \frac{1}{\chi(z)} - \frac{1}{\chi(z')} \right], \quad (13)$$

where  $\chi(z) = \int_0^z dz''/H(z'')$  is the radial comoving distance.

Besides the quasar sample in the whole redshift region, we are also interested in the quasar subsamples in the low redshift  $z < 1.5$  and the high redshift  $z > 1.5$ . In the “All-All” subsample, there are  $N_{lq1} \approx 3.54 \times 10^5$  QSOs at low redshifts  $z < 1.5$  (“All-Low”) and  $N_{hq1} \approx 6.57 \times 10^5$  QSOs at  $z > 1.5$  (“All-High”). The mean redshifts are 0.90 and 2.28, respectively. For the “UVX-All” subsample, we are left with  $N_{lq2} \approx 2.87 \times 10^5$  (“UVX-Low”) and  $N_{hq2} \approx 3.21 \times 10^5$  (“UVX-High”) quasars. Their mean redshifts are 0.90 and 2.02, respectively.

In these four cases, we also assume that the theoretical redshift distributions are approximated by the function Eq. (11) in the redshift region  $[z_1, z_2]$ . Furthermore, we widen these redshift distributions by two one-tailed Gaussians when  $0 \leq z < z_1$  and  $z > z_2$  [47]:

$$\frac{dN}{dz}(z) = [z_1, z_2] \exp \left[ -\frac{(z - [z_1, z_2])^2}{2\sigma^2} \right], \quad (14)$$

where  $\sigma$  is the dispersion between photometric and spectroscopic redshifts. This technique of widening by Gaussians is consistent with determining  $dN/dz$  from spectroscopic matches in the photometric redshift bin [47]. In Ref. [47], the authors measured this dispersion in the different redshift bins and found  $\sigma \sim 0.2$ . Therefore, in our following calculations we simply set  $\sigma = 0.2$ .

We have explicitly checked that these choices for the parameters  $\alpha$  and  $\sigma$  have negligible impact on our final results.

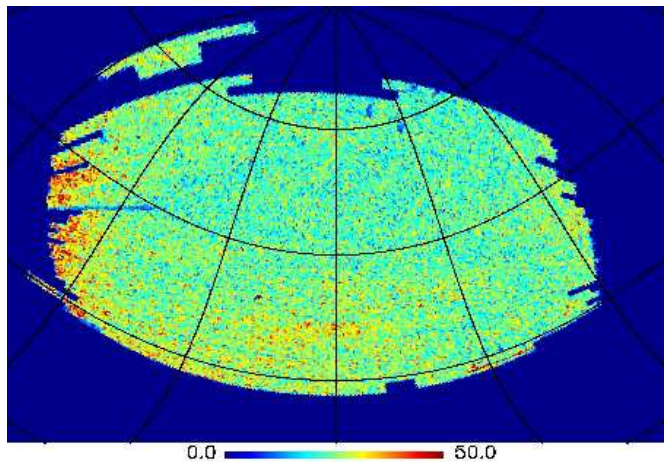


FIG. 2: Zoom on the SDSS DR6-QSO number density map with  $N_{\text{side}} = 128$  for the “All-All” subsample. This map is in celestial coordinates. The grid spacing is  $30^\circ$  and the center is at RA = 180 deg, Dec = 37 deg, corresponding to  $l = 167.45$  and  $b = 75.3$  degrees in Galactic coordinates. RA is increasing to the left.

#### IV. DR6-QSO AUTO-CORRELATION FUNCTION

In this section we will use DR6-QSO sample to compute the QSO auto correlation function (ACF).

##### A. QSO Pixelation

We pixelate the quasar maps using the HEALPix software package<sup>3</sup> [48]. We use a relatively coarse resolution:  $N_{\text{side}} = 64$ , corresponding to  $N_{\text{pix}} = 49,152$  pixels with dimensions  $0.92^\circ \times 0.92^\circ$ . This resolution is sufficient for the large scale correlations we are interested in. In Fig.2, for illustrative purposes, we show the quasar number density map of the “All-All” subsample in celestial coordinates. For the lowest resolution map, there are only  $\sim 20\%$  of these pixels actually contain quasar sources.

In the low resolution map ( $LN_{\text{side}} = 64$ ), there are many edge pixels which are only partially filled by the QSOs. To account for such an effect, following Ref. [13], we also use a higher resolution pixelation map ( $HN_{\text{side}} = 512$ ) to estimate the coverage fraction of each edge pixel. In order to determine the mask of the actual sky coverage of the DR6 survey, we generate a random sample of galaxies using the DR6 database to ensure roughly uniform sampling on the SDSS CasJobs website<sup>4</sup>. By using a sufficiently large number of random galaxies (between

<sup>3</sup> Available at <http://healpix.jpl.nasa.gov/>.

<sup>4</sup> Available at <http://casjobs.sdss.org/CasJobs/default.aspx/>.

13–20 million) we can make sure to have a good sampling when these are pixelated on the high resolution map.

Here, we choose  $LN_{\text{side}} = 64$  and  $HN_{\text{side}} = 512$  for the low and high resolution maps, respectively. We estimate the coverage fraction of each low resolution pixel,  $f_i$ , as:

$$f_i = \frac{N_{\text{mask}}^{\text{high}}(i)}{64}, \quad (15)$$

where  $N_{\text{mask}}^{\text{high}}(i)$  is the number of high resolution pixels within the mask for each coarse pixel  $i$ , and for choice made here there are  $64 = (HN_{\text{side}}/LN_{\text{side}})^2 = (512/64)^2$  high resolution pixels in each coarse pixel. Using this method now most of edge pixels are partially covered by the SDSS DR6 survey,  $0 < f_i < 1$ .

We then correct the maps by dividing the observed number of quasars in each coarse pixel by the fraction of the sky within the pixel that was observed, yielding  $n_i/f_i$ . We use the higher resolution to calculate the average number of quasars per coarse pixel,  $\bar{n}$ :

$$\bar{n} = \frac{N_q}{\sum N_{\text{mask}}^{\text{high}}(i)} \times 64 = \frac{N_q}{\sum f_i}. \quad (16)$$

We also use a higher low-resolution  $LN_{\text{side}} = 128$  and a higher high-resolution  $HN_{\text{side}} = 1024$  to perform all the calculations and find that our results are stable.

## B. ACF Estimator

In order to measure the DR6-QSO ACF, we use the ACF estimator  $\hat{c}^{tt}(\theta)$ , where the index  $tt$  refers to the total catalog (including possible stellar contaminations):

$$\hat{c}^{tt}(\theta) = \frac{1}{N_\theta} \sum_{i,j} \frac{(n_i - f_i \bar{n})(n_j - f_j \bar{n})}{\bar{n}^2}, \quad (17)$$

$$N_\theta = \sum_{i,j} f_i f_j, \quad (18)$$

where  $f_i$  is the pixel coverage fraction,  $n_i$  is the number of quasar sources in each pixel, and  $\bar{n}$  is the expectation value for the number of objects in the pixel. The sum runs over all the pixels with a given angular separation. For each angular bin centered around  $\theta$ ,  $N_\theta$  is the number of pixels pairs separated by an angle within the bin, weighted with the coverage fractions.

This estimator is equivalent to the one used in Ref. [49] in which the authors construct the ACF from the counts of data-data, random-data and random-random number density pairs:

$$\hat{c}^{tt}(\theta) = \frac{QQ(\theta) + RR(\theta) - 2QR(\theta)}{RR(\theta)}, \quad (19)$$

where  $Q$  and  $R$  denote the data point and random point, respectively. In the following calculations, we also use this estimator for cross-checking and find consistent results.

Because we pixelate the quasar map using a low resolution  $N_{\text{side}} = 64$ , in which the pixel size is  $55'$  [48], we use  $N_b = 12$  angular bins in the range  $1^\circ \leq \theta \leq 12^\circ$  and a linear binning in our calculation. The choice of binning does not affect the results significantly.

## C. Covariance Estimator

We estimate the covariance matrix of the data points using jackknife resampling method [50]. This method is to divide the data into  $M$  patches, then create  $M$  subsamples by neglecting each patch in turn. These patches have roughly equal area. In practice, we firstly list the whole set of pixels covered by the survey, and then divide them into  $M = 30$  patches that do not have very similar shape, but have roughly equal area (i.e. equal number of pixels).

The covariance estimator reads:

$$C_{ij} = \frac{M-1}{M} \sum_{k=1}^M \left[ \hat{C}_k^{tt}(\theta_i) - \bar{C}^{tt}(\theta_i) \right] \left[ \hat{C}_k^{tt}(\theta_j) - \bar{C}^{tt}(\theta_j) \right], \quad (20)$$

where  $\hat{C}_k^{tt}(\theta_i)$  are the observed ACF of the  $M$  subsamples in the  $i$ -th angular bin and  $\bar{C}^{tt}(\theta_i)$  are the mean ACF over  $M$  realizations. The diagonal part of these matrices gives the variance of the ACF in each bin  $C_{ii}^k = \sigma_i^2$ , while the off-diagonal part represents the covariance between the angular bins. We also change the number of patches  $M$  and verify that the covariance matrix is stable. We refer the readers to Ref. [14] for a more extensive comparison between several covariance estimators.

## D. Stellar Contamination

Although the SDSS DR6-QSO catalog we use has very high efficiency in the selection algorithm, stars are point-like sources that inevitably contaminate the catalog. An estimate of the level of stellar contamination can be computed using the fact that the correlations properties of stars are very different from those of QSOs. In particular, a nearly flat contribution, up to large angular scales (that correspond to small physical Galactic distances) is expected from stars of our own galaxy.

If we substitute  $n_i \rightarrow an_i^q + (1-a)n_i^s$ , where  $a$  is the efficiency of the quasar catalog, the ACF estimator of Eq. (17) becomes:

$$\hat{c}^{tt}(\theta) = a^2 \hat{c}^{qq}(\theta) + (1-a)^2 \hat{c}^{ss}(\theta) + \epsilon(\theta), \quad (21)$$

where  $\hat{c}^{qq}(\theta)$  and  $\hat{c}^{ss}(\theta)$  are the intrinsic ACF of QSOs and stars, respectively, and  $\epsilon(\theta)$  is a tiny offset arising from cross-terms [47]:

$$\begin{aligned} \epsilon(\theta) &= 2(a-a^2) \left( \frac{QS(\theta) + RR(\theta) - QR(\theta) - SR(\theta)}{RR(\theta)} \right), \\ &= \frac{2(a-a^2)}{N_\theta} \sum_{i,j} \frac{(n_i^q - f_i \bar{n})(n_j^s - f_j \bar{n})}{\bar{n}^2}. \end{aligned} \quad (22)$$

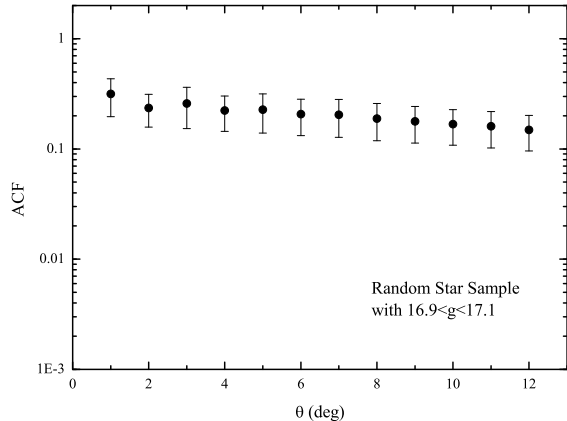


FIG. 3: The auto-correlation function of star catalog  $\hat{c}^{ss}(\theta)$ . And the errors are also derived from the jackknife method.

If the efficiency of the catalog is high enough, i.e.  $a > 90\%$ , this cross-term  $\epsilon(\theta)$  should be close to zero and can be neglected safely in the analysis. Otherwise,  $\epsilon(\theta)$  will become large and is comparable to the intrinsic ACF of stars  $\hat{c}^{ss}(\theta)$ . Thus, in order to correctly determine the efficiency of the catalog with a large stellar contamination, such as the “All-All” subsample, we have to take this term into account. We will show this effect in the following sections.

To compute the stellar contamination, we extract a large number ( $\sim 8 \times 10^4$ ) of stars in SDSS DR6 survey in the magnitude range  $16.9 < g < 17.1$  from the CasJobs website and compute the ACF of stars  $\hat{c}^{ss}(\theta)$  using Eq. (17). In Fig. 3 we show the stellar ACF and its errors which are also measured with the jackknife method. We can find that the stellar contamination will dominate the ACF of the total catalog at the largest scales where the ACF of QSOs  $\hat{c}^{qq}(\theta) \rightarrow 0$ . The star contribution is indeed not perfectly flat and retains a small slope even at large angles, dropping from  $\hat{c}^{ss}(1^\circ) \sim 0.3$  to  $\hat{c}^{ss}(12^\circ) \sim 0.15$ , which is consistent with the result of Ref. [47], showing that probably our star catalog is also contaminated at some level by QSOs. However, the contribution at large angular scales could be robustly estimated and removed.

### E. Systematic Errors

Several systematics effects, including the galactic extinction by dust, sky brightness, number of point sources and poor seeing, could potentially affect both the observed ACF and CCF. These systematics are investigated in detail in Refs. [13, 15, 47]. We also checked for their contribution in our calculation and in particular we consider extinction and point sources contamination, that

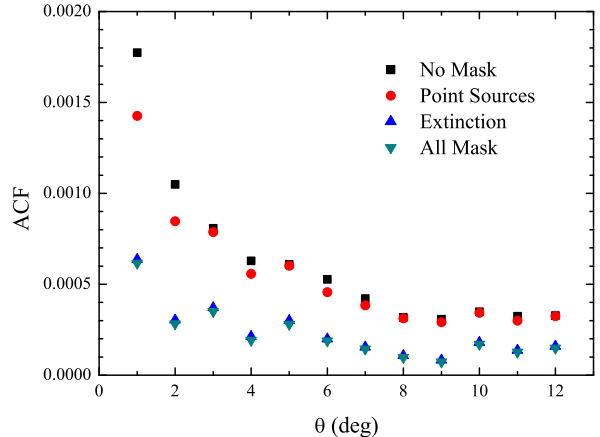


FIG. 4: The auto-correlation function of quasar “UVX-All” subsample measured for all the sample, for a single foreground mask and for all masks joint. No error bars are reported.

are believed to affect most the measured correlations.

Basically we recompute the ACF by considering only objects within the pixels with  $A_g < 0.18$  (the g-band Galactic extinction) for the reddening, while for the point sources we remove the pixels with more than twice average number density of sources,  $n_i < 2\bar{n}$ . These masks will remove about  $\sim 20\%$  of the considered area. Among these two systematics we find that the extinction have the major effect on the derived ACF and we plot the observed ACF with and without these foreground masks for the “UVX-All” subsample in Fig.4. We also plot the effect of extinction on the ACF for the “UVX-Low” and “UVX-High” subsamples in Fig.5. Therefore, we will use the extinction mask  $A_g < 0.18$  only in our following analysis. Our results are in quantitative agreement with those of Ref. [13] based on SDSS DR4 quasar catalog.

### F. Auto-Correlation Functions

In this subsection, we summarize the whole calculations of DR6-QSO ACF. For our purpose we construct six different quasar subsamples from the SDSS DR6-QSO catalog. Firstly we pixelate the quasar maps using HEALPix software and remove the  $\sim 20\%$  highest contaminated pixels with  $A_g > 0.18$ . Next we use the ACF estimator Eq. (17) and the covariance estimator Eq. (20) to calculate the ACF and its covariance matrix for each quasar subsample. Finally we consider the contribution of stellar contamination and also the cross terms when the efficiency is not high enough. Note that in the following analysis we take in account the window function  $w(\theta)$  associated with our pixelation.

In Fig. 6 we plot the observed ACF for these six different quasar subsamples. We find that for the “UVX-All”

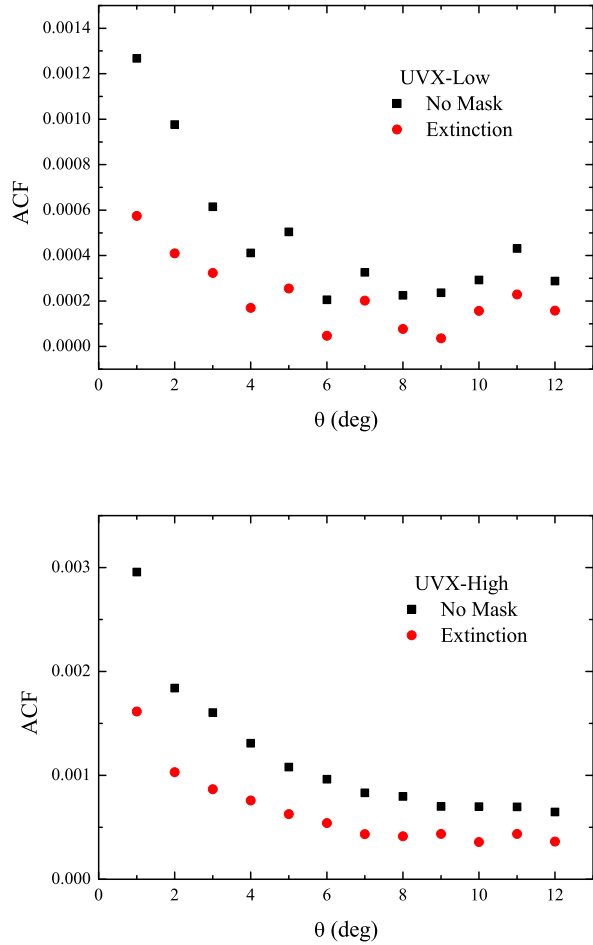


FIG. 5: The auto-correlation function of quasar “UVX-Low” and “UVX-High” subsamples measured for the extinction mask. No error bars are reported.

subsample the values of ACF are consistent with previous works [13, 14]. However, if we consider the high redshift subsample, the observed ACF becomes large. The reason is that in this case the subsample has a higher mean redshift. At this high mean redshift, the bias and stellar contamination will become larger and produce a larger ACF (the efficiency is smaller). Moreover, due to their higher mean redshift, larger bias and smaller efficiency, three “All- $\times \times \times$ ” subsamples also have larger observed ACFs than the corresponding three “UVX- $\times \times \times$ ” subsamples. In Fig.6 we show the theoretical ACFs for different cases. Obviously all the plots depend on the chosen cosmology. Here we use the best fit model of WMAP five-year data [1]:  $\Omega_b h^2 = 0.02267$ ,  $\Omega_c h^2 = 0.1131$ ,  $\tau = 0.084$ ,  $h = 0.705$ ,  $n_s = 0.96$  and  $A_s = 2.15 \times 10^{-9}$  at  $k = 0.05 \text{ Mpc}^{-1}$ . For the other two free parameters, bias and efficiency, we choose the best fit values of Table II, obtained from our calculations in the  $\Lambda$ CDM framework

that will be shown in the following sections. We find that there is good agreement between the theory from the WMAP5 best fit model and the observed ACF in each quasar subsample.

## V. QSO-CMB CROSS-CORRELATION FUNCTION

For the cross-correlation analysis, we use the WMAP Internal Linear Combination (ILC) map derived from the five-year WMAP data, with  $HN_{\text{side}} = 512$  provided by the WMAP team [51], shown in Fig.7, in the same region as the SDSS DR6-QSO data. This ILC map was already built to minimize the Galactic and other foreground contaminations. In our calculations, we downgrade the ILC map to the low resolution  $LN_{\text{side}} = 64$ . For the WMAP mask, we use the “KQ75” mask [52] corresponding roughly to the “Kp0” cut in the three-year data release. This mask map has also  $N_{\text{side}} = 512$ . We downgrade this map to the low resolution and set the weight  $w^T = 0$  for all pixels including at least one masked high resolution pixel [7].

To measure the CCF between the SDSS DR6-QSO number density map and the WMAP ILC map, we rely on the following estimator:

$$\hat{c}^{tT}(\theta) = \frac{1}{N_\theta} \sum_{i,j} (T_i - \bar{T}) \frac{n_j - f_j \bar{n}}{\bar{n}}, \quad (23)$$

where  $T_i$  is the CMB temperature in the  $i$ -th pixel and  $\bar{T}$  is the mean (monopole) value for the CMB temperature in the unmasked area.  $N_\theta$  is the number of pixels pairs, which has been defined in the previous Section. We also use  $N_b = 12$  angular bins in the range  $1^\circ \leq \theta \leq 12^\circ$  and a linear binning in our calculation. We also check the contributions from the extinction and point sources contamination in Fig.9, and find that the extinction have the major effect on the CCF. We also plot the effect of extinction on the CCF for the “UVX-Low” and “UVX-High” subsamples in Fig.10. Therefore, we apply the reddening mask with  $A_g < 0.18$  to be consistent with the ACF measurements.

We also consider the possible contributions from stars in the CCF calculations. The stellar contamination has to be subtracted from the total CCF and the QSO-temperature correlation that will be compared with the theoretical models becomes:

$$\hat{c}^{qT}(\theta) = \frac{\hat{c}^{tT}(\theta) - (1-a)\hat{c}^{sT}(\theta)}{a}, \quad (24)$$

where the star-temperature cross-correlation has to be also estimated.

The covariance matrices are also calculated by using jackknife resampling method, Eq. (20). We firstly list all the pixels covered by the survey in the quasar map, and divide them into  $M = 30$  patches. Then we create  $M$

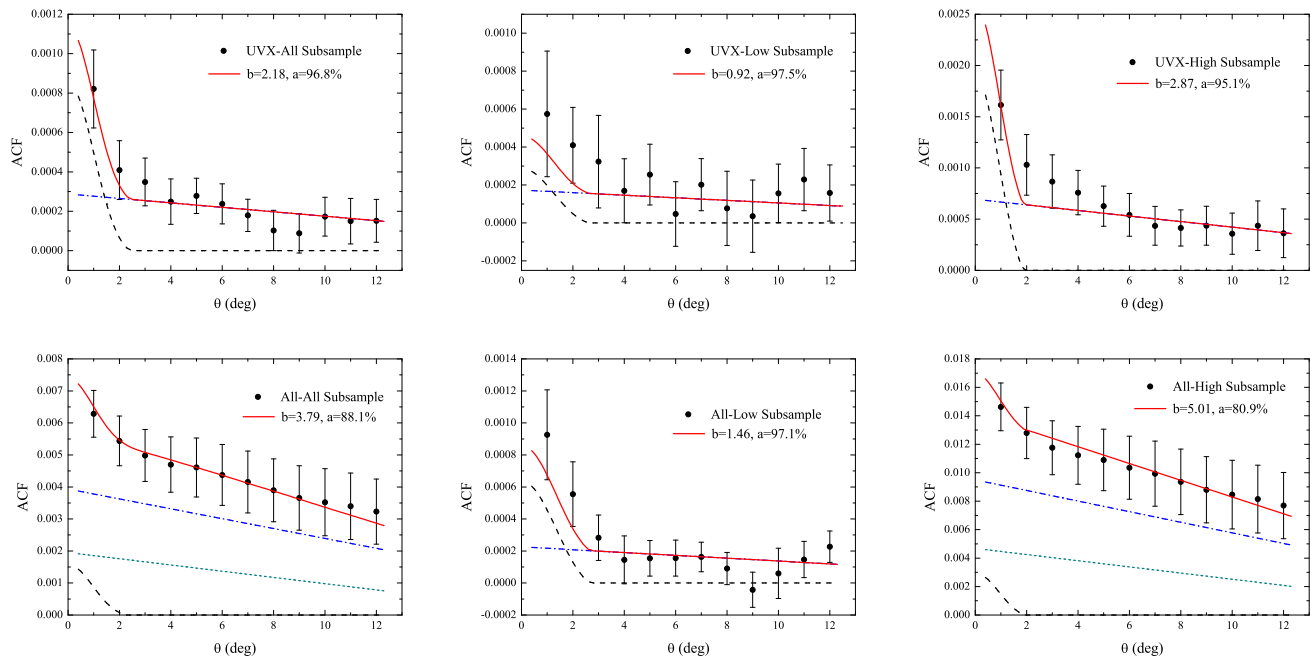


FIG. 6: The observed auto-correlation function (ACF) of different quasar subsamples. Top three panels are for “UVX-All”, “UVX-Low” and “UVX-High” subsamples. Bottom three panels are for “All-All”, “All-Low” and “All-High” subsamples. All errors are estimated with jackknife method. The red solid lines are the theoretical predictions from the best fit model of WMAP five-year data, while the black dashed lines and the blue dash-dot lines are its component (theoretical quasars ACF and stellar contamination). We also plot the contributions from the cross term  $\epsilon(\theta)$  (cyan short dashed lines) in the “All-All” and “All-High” subsamples in which the efficiencies become small.

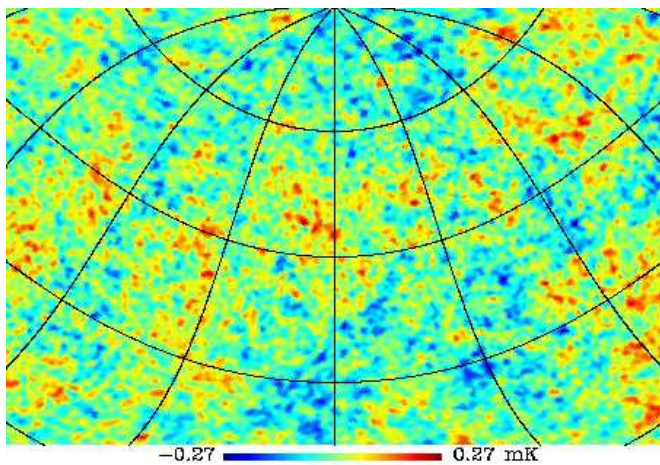


FIG. 7: WMAP Internal Linear Combination map with  $N_{\text{side}} = 128$  in celestial coordinates zoomed on the same region probed by SDSS DR6-QSOs. The grid spacing and center are the same as in Fig.2.

subsamples by neglecting each patch in turn and discard the same pixels in the WMAP ILC map.

In Fig. 8 we plot the observed CCF for these six different quasar subsamples, together with the theoretical

CCF predictions of WMAP5 best fit cosmological model. There is good agreement between the theoretical and observed CCFs.

The values of CCF of the “UVX-All” subsample are consistent with previous works [13, 14]. We find  $0.22 \pm 0.10 \mu\text{K}$  and  $0.26 \pm 0.09 \mu\text{K}$  for the “UVX-All” and “All-All” subsamples at 1 deg, respectively. The median value of “All-All” subsample is larger than one of “UVX-All”, due to the larger bias and stellar contamination. The larger number of quasars in “All-All” subsample allow to slightly shrink the error bars. In particular, we find that the high redshift subsample  $z > 1.5$  also gives a non-vanishing cross-correlation signal, which is consistent with the results of Ref. [15]. One of the possible reasons could be that the high redshift subsample has a larger bias and stellar contamination. Another speculative possibility is also that a larger value for the ISW CCF than that implied by  $\Lambda\text{CDM}$  could reflect a different underlying cosmological model, characterized by an early departure from matter dominance and onset of acceleration, as it happens in early dark energy and modified gravity scenarios.

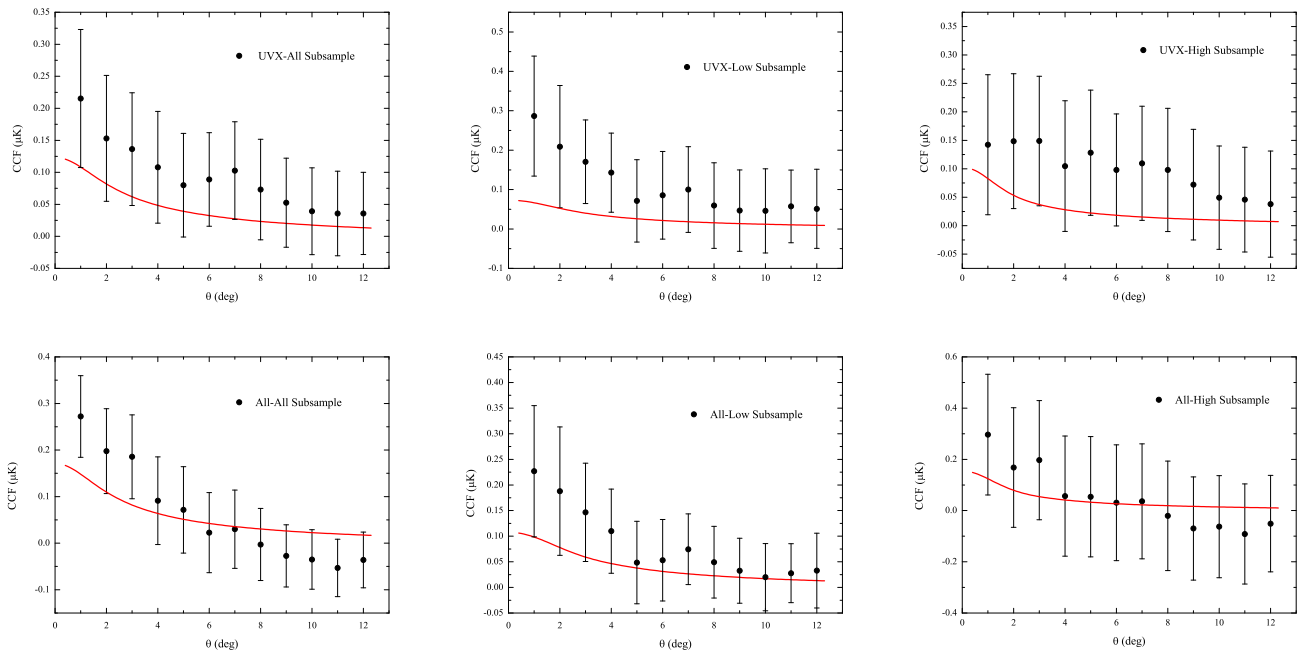


FIG. 8: The observed cross-correlation function (CCF) between different quasar subsamples and WMAP ILC map. Top three panels are for “UVX-All”, “UVX-Low” and “UVX-High” quasar subsamples. Bottom three panels are for “All-All”, “All-Low” and “All-High” quasar subsamples. All errors are jackknife estimated. The red solid lines are the theoretical predictions from the best fit model of WMAP five-year data.

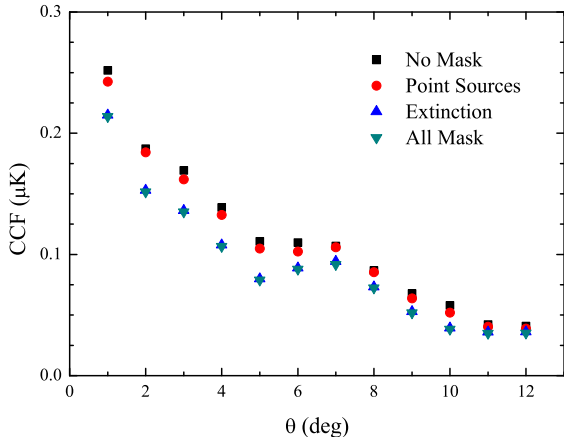


FIG. 9: The cross-correlation function of quasar “UVX-All” subsample measured for all the sample, for a single foreground mask and for all masks joint. No error bars are reported.

## VI. METHOD AND DATASETS

### A. Parametrization of Early Dark Energy

Due to the possible non-zero ISW signal at high redshift provided by the early dark energy model, we will also consider here the EDE mocker model introduced in Ref. [54]:

$$w_{\text{EDE}}(a) = -1 + \left[ 1 - \frac{w_0}{1 + w_0} a^C \right]^{-1}, \quad (25)$$

where  $a = 1/(1+z)$  is the scale factor,  $w_0$  is the present equation-of-state of dark energy and  $C$  characterizes the “running” of the equation of state. Consequently, the evolution of dark energy density can easily be obtained via energy conservation as:

$$\frac{\rho_{\text{EDE}}(a)}{\rho_{\text{EDE}}(1)} = [(1 + w_0)a^{-C} - w_0]^{3/C}. \quad (26)$$

In Fig. 11 we plot the dark energy density (upper part of the panel) and equation of state (bottom part of the panel) as a function of redshift for two different models: pure  $\Lambda$ CDM (blue lines) and EDE (red lines) which has  $(w_0, C) = (-0.95, 2.50)$ . All these models fit the CMB and the lower redshift SNIa constraints very well [41]. In the panel we also show as a shaded vertical band the region in the redshift range  $z = 0 - 5$ . This is the redshift

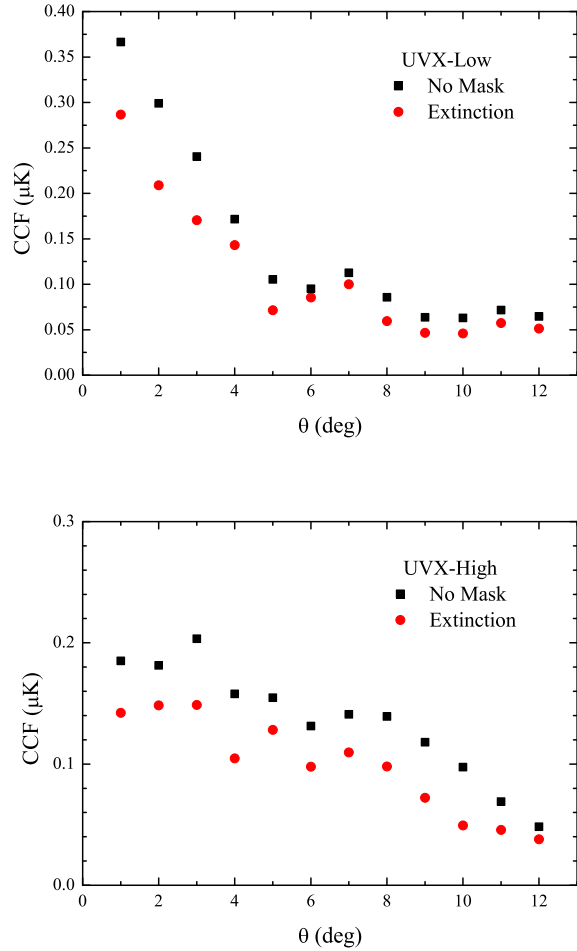


FIG. 10: The cross-correlation function of quasar “UVX-Low” and “UVX-High” subsamples measured for the extinction mask. No error bars are reported.

range we will be (mainly) focussing on in the rest of the paper.

We stress that this is just one of the possible parameterizations for early dark energy models, another one has been suggested by Ref. [53] and recently used in Ref. [40]. However, we prefer to use the mocker model in order to compare with the findings of Ref. [54] and because this parametrization has a smooth redshift derivative at low  $z$  for  $w(z)$ . We note that one of the most important parameters is the amount of dark energy during the structure formation period and this is given by ( $a_{\text{eq}}$  is the matter-radiation equality scale factor):

$$\Omega_{\text{EDE,sf}} = -(\ln a_{\text{eq}})^{-1} \int_{\ln a_{\text{eq}}}^0 \Omega_{\text{EDE}}(a) d \ln a, \quad (27)$$

and we will also quote this value in the rest of the paper in order to compare with other works and constraints as well (e.g. Refs. [28, 34]).

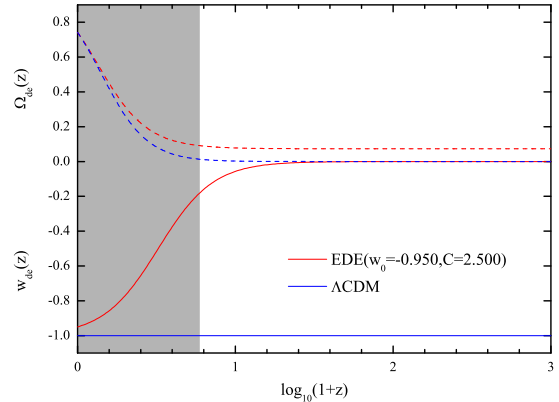


FIG. 11: The evolution of dark energy density and equation of state for two models,  $w_0 = -0.95$  and  $C = 2.5$  (EDE) and pure  $\Lambda$ CDM model. The shaded area represents the redshifts that is probed by SDSS DR6-QSOs ( $z \sim 0 - 5$ ).

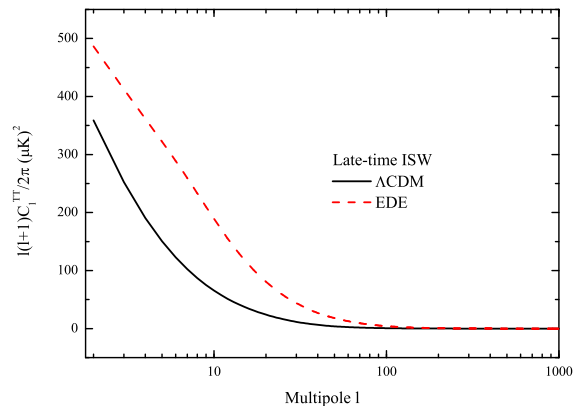


FIG. 12: The late-time ISW temperature power spectrum in two different dark energy models:  $w_0 = -0.95$  and  $C = 2.5$  (EDE) and pure  $\Lambda$ CDM model.

In Fig. 12 we plot the late-time ISW temperature power spectrum in the two different dark energy models analyzed. We find that the early dark energy model produces a larger contribution to the CMB primary power spectrum at low multipoles than the  $\Lambda$ CDM model due to the different low redshift evolution: differences up to a factor  $\sim 2$  are present for  $l$  values smaller than 10, reflecting the fact that ISW cross-correlation is in place earlier than in  $\Lambda$ CDM, due to the early departure from matter dominated expansion rate.

We also focus on the ISW effect at different redshifts investigating EDE models. We modified the CAMB code [55] to calculate the contributions of ISW effect to the

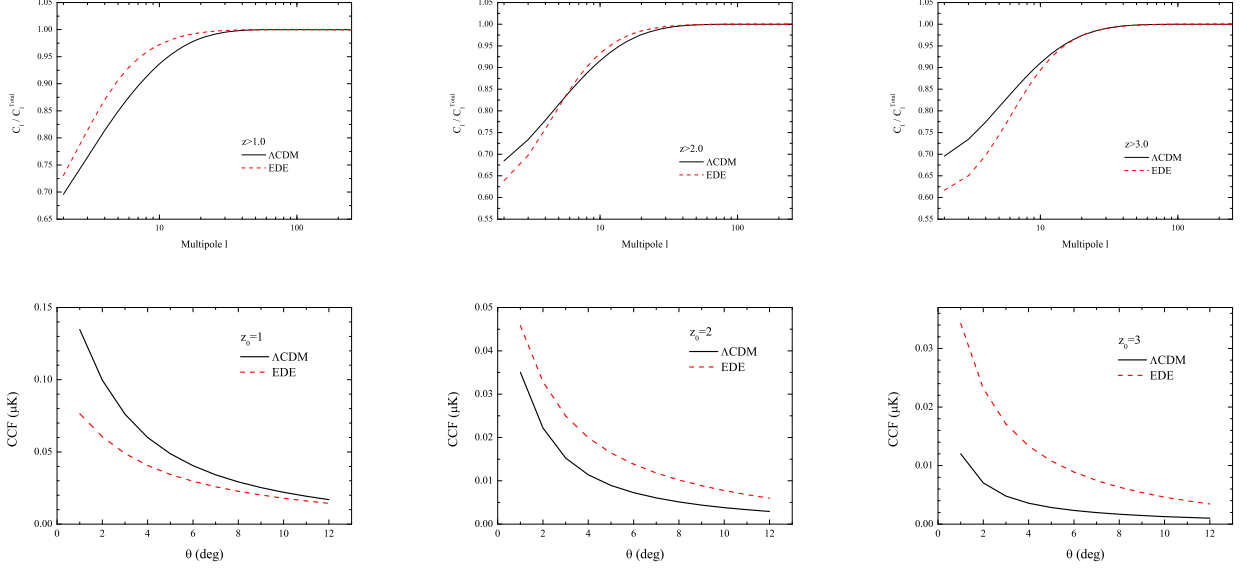


FIG. 13: Top: Ratio of the CMB temperature power spectrum with and without the ISW effect at different low redshifts in two different dark energy models: EDE (red dashed lines) and  $\Lambda\text{CDM}$  (black solid lines). Bottom: The cross-correlation functions  $C^{gT}(\theta)$  between EDE Mocker model (red dashed lines) and pure  $\Lambda\text{CDM}$  model (black solid lines). The redshift distribution  $dN/dz$  is assumed to be a Gaussian function centered at three different mean redshifts  $z_0 = 1, 2, 3$  comparison with a  $\sigma = 0.5$ . We fix bias to  $b = 2.2$  for illustrative purpose.

power spectrum prior to some redshifts  $z_*$ , and neglect the ISW effect at low redshifts:

$$\frac{\Delta T}{T}^{\text{ISW}}(\hat{\mathbf{n}}) = 0, \text{ when } z < z_*. \quad (28)$$

In Fig. 13 we plot the ratio of the CMB temperature power spectra with and without the ISW effect at different low redshifts and in two different dark energy models. We find that at the lowest redshift  $z < 1$ , the ISW contribution of  $\Lambda\text{CDM}$  is larger than the EDE model. However, when the redshift becomes larger, the EDE model contributes more to the ISW effect and to the CMB temperature power spectrum. Therefore, when calculating the cross-correlation power spectra between ISW and QSO survey with different mean redshifts, we can see that the higher the mean redshift of QSO survey is, the larger the cross-correlation  $C_l^{\text{qT}}$  becomes, which is shown in Fig. 13. From these plots it is clear how the cross-correlation signal between QSO number density and CMB temperature differs in the two models up to a factor three (the differences at higher redshifts  $z > 3$  becoming even larger than those shown here). Moreover, the redshift evolution of the ISW signal is quite different in the two models and this is promising for future studies that aim at investigating high-redshift deviations from the standard model.

## B. ISW Likelihood Function

In Refs. [13, 14], the authors firstly used the QSO ACF data only to determine the bias  $b$ , when fixing the other parameters and then they used the CMB-QSO CCF data to constrain the significance of ISW signal or other cosmological parameters. However, in order to make the whole analysis consistent, in our calculations we use both the ACF and CCF data to constrain all the parameters, including the bias  $b$ , efficiency  $a$ , ISW amplitude  $A_{\text{amp}}$ , which is defined in Eq. (33), and other cosmological parameters, simultaneously.

We then compare the theoretical ACF  $c^{\text{qq}}(\theta)$  and CCF  $c^{\text{qT}}(\theta)$  with the observed values of ACF  $\hat{c}^{\text{qq}}(\theta)$  and CCF  $\hat{c}^{\text{qT}}(\theta)$ , respectively, through the Gaussian likelihood function:

$$\begin{aligned} \mathcal{L}_{\text{ACF}} &= (2\pi)^{-N/2} [\det C_{ij}]^{-1/2} \\ &\times \exp \left[ - \sum_{i,j} \frac{C_{ij}^{-1} (\hat{c}_i^{\text{qq}} - c_i^{\text{qq}})(\hat{c}_j^{\text{qq}} - c_j^{\text{qq}})}{2} \right], \quad (29) \end{aligned}$$

$$\begin{aligned} \mathcal{L}_{\text{CCF}} &= (2\pi)^{-N/2} [\det C'_{ij}]^{-1/2} \\ &\times \exp \left[ - \sum_{i,j} \frac{C'_{ij}{}^{-1} (\hat{c}_i^{\text{qT}} - c_i^{\text{qT}})(\hat{c}_j^{\text{qT}} - c_j^{\text{qT}})}{2} \right] \quad (30) \end{aligned}$$

where  $C_{ij}$  and  $C'_{ij}$  are the DR6-QSO auto-correlation function and CMB-QSO cross-correlation function covariance matrix.

### C. Other Current Datasets

Besides the ACF and CCF data, we will rely here on the following cosmological probes: i) CMB anisotropies and polarization; ii) baryonic acoustic oscillations in the galaxy power spectra; iii) SNIa distance moduli.

In the computation of CMB power spectra we have included the WMAP five-year (WMAP5) temperature and polarization power spectra with the routines for computing the likelihood supplied by the WMAP team [1, 51, 52, 56, 57, 58].

BAOs (Baryonic Acoustic Oscillations) have been detected in the current galaxy redshift survey data from the SDSS and the Two-degree Field Galaxy Redshift Survey (2dFGRS) [59, 60, 61, 62]. The BAO can directly measure not only the angular diameter distance,  $D_A(z)$ , but also the expansion rate of the universe,  $H(z)$ , which is powerful for studying dark energy [63]. Since current BAO data are not accurate enough for extracting the information of  $D_A(z)$  and  $H(z)$  separately [64], one can only determine an effective distance [59]:

$$D_v(z) \equiv \left[ (1+z)^2 D_A^2(z) \frac{cz}{H(z)} \right]^{1/3}. \quad (31)$$

In this paper we use the Gaussian priors on the distance ratios  $r_s(z_d)/D_v(z)$ :

$$\begin{aligned} r_s(z_d)/D_v(z=0.20) &= 0.1980 \pm 0.0058, \\ r_s(z_d)/D_v(z=0.35) &= 0.1094 \pm 0.0033, \end{aligned} \quad (32)$$

with a correlation coefficient of 0.39, extracted from the SDSS and 2dFGRS surveys [62], where  $r_s$  is the comoving sound horizon size and  $z_d$  is drag epoch at which baryons were released from photons given by Ref. [65].

The SNIa data provide the luminosity distance as a function of redshift which is also a very powerful measurement of dark energy evolution. The supernovae data we use in this paper are the recently released Union compilation (307 samples) from the Supernova Cosmology project [2], which include the recent samples of SNIa from the (Supernovae Legacy Survey) SNLS and ESSENCE survey, as well as some older data sets, and span the redshift range  $0 \lesssim z \lesssim 1.55$ . In the calculation of the likelihood from SNIa we have marginalized over the nuisance parameter as done in Ref. [66].

Furthermore, we make use of the Hubble Space Telescope (HST) measurement of the Hubble parameter  $H_0 \equiv 100 h \text{ km s}^{-1} \text{ Mpc}^{-1}$  by a Gaussian likelihood function centered around  $h = 0.72$  and with a standard deviation  $\sigma = 0.08$  [67].

### D. Future Datasets

In order to forecast future measurements we will use the same observables as before without BAO.

TABLE I. Assumed experimental specifications for the mock Planck-like measurements. The noise parameters  $\Delta_T$  and  $\Delta_P$  are given in units of  $\mu\text{K-arcmin}$ .

$f_{\text{sky}}$	$l_{\text{max}}$	(GHz)	$\theta_{\text{fwhm}}$	$\Delta_T$	$\Delta_P$
0.65	2500	100	9.5'	6.8	10.9
		143	7.1'	6.0	11.4
		217	5.0'	13.1	26.7

For the simulation with Planck [68], we follow the method given in Ref. [69] and mock the CMB temperature (TT) and polarization (EE) power spectra and temperature-polarization cross-correlation (TE) by assuming a given fiducial cosmological model. In Table I, we list the assumed experimental specifications of the future (mock) Planck measurement.

The proposed satellite SNAP<sup>5</sup> (Supernova / Acceleration Probe) will be a space based telescope with a one square degree field of view that will survey the whole sky. It aims at increasing the discovery rate of SNIa to about 2000 per year in the redshift range  $0.2 < z < 1.7$ . In this paper we simulate about 2000 SNIa according to the forecast distribution of the SNAP [70]. For the error, we follow the Ref. [70] which takes the magnitude dispersion to be 0.15 and the systematic error  $\sigma_{\text{sys}} = 0.02 \times z/1.7$ . The whole error for each data is given by  $\sigma_{\text{mag}}(z_i) = \sqrt{\sigma_{\text{sys}}^2(z_i) + 0.15^2/n_i}$ , where  $n_i$  is the number of supernovae of the  $i$ 'th redshift bin.

For the future ISW ACF and CCF data, we simulate two mock datasets from the best fit values of data combination WMAP5+BAO+SNIa+“UVX-All” in the  $\Lambda$ CDM and EDE models, respectively. We also set  $b = 2.0$ ,  $a = 97\%$  and  $A_{\text{amp}} = 1$  with error bars on these parameters that are reduced by a factor three. We use directly the covariance matrix taken from present data and divide it by a factor nine. This improvement could be achievable by next generation of large-scale surveys such as the Large Synoptic Survey Telescope (LSST, [71]), the Panoramic Survey Telescope and Rapid Response System (Pan-STARRS, [72]) and the Dark Energy Survey (DES; The Dark Energy Survey Collaboration 2005) are likely to allow for an order of magnitude improvement in the number of QSOs which will account for the factor three considered here. Also, the coverage of the sky fraction is at present of the order of 20% by SDSS DR6, so an all-sky survey will already give a factor two improvement (we assume that the error bars scale as  $\sqrt{N_{\text{QSOs}}}$ , which is reasonable if these are independent). Another possible improvement in this direction is the use of type-2 QSOs instead of the type-1 used here that could further decrease the error bars of the sample (see the discussion in [45]).

<sup>5</sup> Available at <http://snap.lbl.gov/>.

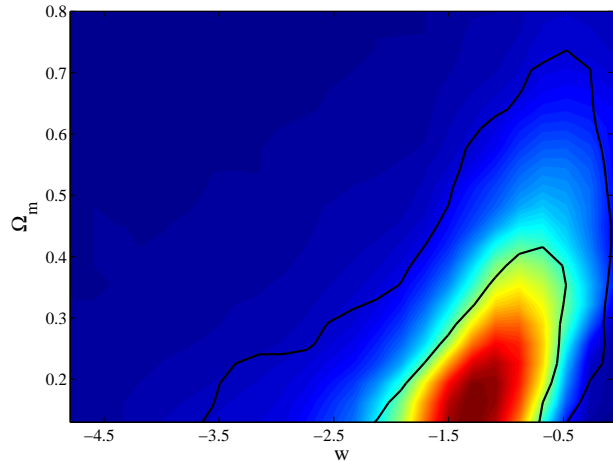


FIG. 14: Two-dimensional (marginalized) contours of  $\Omega_{m0}$  and constant  $w_{DE}$  from the ISW data only.

## VII. NUMERICAL RESULTS

In our analysis, we perform a global fitting using the `CosmoMC` package [73] a Monte Carlo Markov Chain (MCMC) code, which has been modified to calculate the theoretical ACF and CCF. We assume purely adiabatic initial conditions and a flat universe, with no tensor contribution. We vary the following cosmological parameters with top-hat priors: the dark matter energy density  $\Omega_c h^2 \in [0.01, 0.99]$ , the baryon energy density  $\Omega_b h^2 \in [0.005, 0.1]$ , the primordial spectral index  $n_s \in [0.5, 1.5]$ , the primordial amplitude  $\log[10^{10} A_s] \in [2.7, 4.0]$  and the angular diameter of the sound horizon at last scattering  $\theta \in [0.5, 10]$ . For the pivot scale we set  $k_{s0} = 0.05 \text{ Mpc}^{-1}$ . When CMB data are included, we also vary the optical depth to reionization  $\tau \in [0.01, 0.8]$ . We do not consider any massive neutrino contribution. From the parameters above the MCMC code derives the reduced Hubble parameter  $H_0$ , the present matter fraction  $\Omega_{m0}$ ,  $\sigma_8$ , and  $\Omega_{EDE, sf}$ , so, these parameters have non-flat priors and the corresponding bounds must be interpreted with some care. There are three more parameters related to the ACF and CCF data: the constant bias  $b$ , the efficiency of quasar catalog  $a$  and the ISW amplitude  $A_{amp}$  which is defined by:

$$\bar{C}^{qT}(\theta) = A_{amp} C^{qT}(\theta), \quad (33)$$

where  $\bar{C}^{qT}$  and  $C^{qT}$  are the observed and theoretical CCF. In addition, `CosmoMC` imposes a weak prior on the Hubble parameter:  $h \in [0.4, 1.0]$ . Furthermore, we also include the perturbations of dynamical dark energy models generally as done in Refs. [74, 75, 76].

TABLE II. The results of quasar bias and efficiency of quasar catalog in two dark energy models.

Subsample	Mean Redshift $\bar{z}$	Bias $b$	Efficiency $a$
$\Lambda$ CDM model			
All-All	1.80	$3.79 \pm 0.34$	$88.1\% \pm 0.5\%$
All-Low	0.90	$1.46 \pm 0.29$	$97.1\% \pm 0.5\%$
All-High	2.28	$5.01 \pm 0.81$	$80.9\% \pm 0.7\%$
UVX-All	1.49	$2.18 \pm 0.22$	$96.8\% \pm 0.5\%$
UVX-Low	0.90	$0.92 \pm 0.30$	$97.5\% \pm 0.8\%$
UVX-High	2.02	$2.87 \pm 0.39$	$95.1\% \pm 0.6\%$
EDE Mocker model			
UVX-All	1.49	$2.33 \pm 0.31$	$96.8\% \pm 0.5\%$
UVX-Low	0.90	$1.05 \pm 0.33$	$97.5\% \pm 0.8\%$
UVX-High	2.02	$2.98 \pm 0.43$	$95.1\% \pm 0.6\%$

### A. ISW Only

Firstly, we use the ACF and CCF data of “UVX-All” subsample only to constrain the dark energy model with a constant equation of state  $w_{DE}$ . Because at present the ISW ACF and CCF data have relatively large error bars that do not allow to use this measurement in a very competitive way compared to other cosmological probes, in our calculation we have fixed the other cosmological parameters to the WMAP5 best fit values, as well as the bias, efficiency and amplitude parameters. In Fig. 14 we plot the two-dimensional constraints on  $(w_{DE}, \Omega_{m0})$ . The results show that the ISW data only could give very weak constraints on the background parameters:  $w_{DE} = -1.24 \pm 0.62$  ( $1\sigma$ ) and the  $2\sigma$  upper limit of  $\Omega_{m0} < 0.55$ , which is consistent with the pure  $\Lambda$ CDM model. This result is also consistent with some previous works [13, 14, 77, 78].

### B. Quasar Bias and Efficiency

In our calculations we simply assume that the quasar bias is constant in the redshift region considered. Table II shows the results of quasar bias and efficiency of six subsamples in two dark energy models.

For the “UVX-All” subsample, we obtain a value for the bias  $b = 2.18 \pm 0.22$  ( $1\sigma$ ) in the  $\Lambda$ CDM framework, also consistent with previous measurements [13, 47, 79, 80]. However, we find that this bias result depends on the dark energy model we choose. In the EDE Mocker model, the bias becomes  $b = 2.33 \pm 0.31$  ( $1\sigma$ ). Thus, the mean value of quasar bias becomes slightly higher in an EDE cosmology by  $\sim 10\%$ . This effect is generally present in the subsamples at different redshifts.

On the other hand, we find that the efficiency of “UVX-All” subsample is  $a = 96.8 \pm 0.5\%$ , also consistent with Ref. [45]. This efficiency does not depend on the different dark energy model, which is reasonable since this is an

TABLE III. Estimates of the quasar bias, from five photometric redshift bins.

Redshift Bins	Mean Redshift $\bar{z}$	Bias $b$
$0.75 < z < 1.25$	1.02	$1.58 \pm 0.39$
$1.25 < z < 1.55$	1.43	$1.85 \pm 0.78$
$1.55 < z < 1.95$	1.73	$2.23 \pm 0.87$
$1.95 < z < 2.20$	2.06	$3.28 \pm 0.86$
$2.20 < z < 4.00$	2.46	$5.29 \pm 1.31$

intrinsic feature of the quasar catalog.

In the high redshift subsample, the quasar bias will also become higher and the efficiency becomes clearly smaller. As we mentioned before, at high redshift the stellar contamination will become large. The cross term  $\epsilon(\theta)$  will be comparable to the star ACF  $\hat{c}^{ss}(\theta)$  in Eq. (21). In order to obtain the correct efficiency, we should consider this cross terms in our calculations. If we neglect this cross term, the efficiency will be incorrectly suppressed, since in this case one should need a larger stellar contamination to contribute more ACF. For example, when using “All-All” subsample to do the calculations, if we neglect the cross terms  $\epsilon(\theta)$ , the efficiency is 82.5%, which is consistent with Ref. [45]. However, if taking  $\epsilon(\theta)$  into account, the efficiency rises to 88.1%.

From the above analysis, we find that the quasar bias could evolve with redshift. Models in which the bias varies with redshift have been proposed and investigated (e.g. Refs. [81, 82]). Here, we also give the constraint on the evolution of the QSO bias with redshift. In our calculation we are not using more sophisticated models as those in Refs. [82, 83, 84]. We only split the whole quasar “UVX-All” subsample into five photometric redshift bins:  $[0.75, 1.25]$ ,  $[1.25, 1.55]$ ,  $[1.55, 1.95]$ ,  $[1.95, 2, 2]$  and  $[2.2, 4.0]$ , containing  $\sim 10^5$  objects each, and assume a constant bias in each of them. Then we calculate their auto correlation function to determine their quasar bias. In this analysis we do not include data at  $z < 0.75$ , since in this low redshift the subsample is highly contaminated by the galaxies [47, 85].

In Table III and Fig. 15 we show the estimates of the quasar bias in these five photometric redshift bins. We find that our results are in overall agreement with previous works [47, 86, 87]. In Fig. 15 we also plot the empirical fit derived by directly measuring the real-space clustering of spectroscopically confirmed QSOs in Ref. [79]. Our results are consistent with this empirical fit very well. Furthermore, this analysis also allow to estimate important quantities such as the mass of the host haloes, QSO duty cycle and the Mass-Luminosity relation (see Ref. [83]).

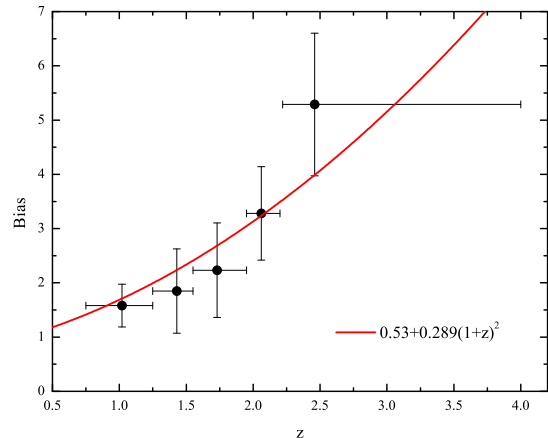


FIG. 15: Estimates of the quasar bias and their  $1\sigma$  error bars from five photometric redshift bins. The red solid line  $b(z) = 0.53 + 0.289(1+z)^2$  is the empirical fit derived by Ref. [79].

### C. Amplitude of ISW Signal

In previous works [14, 15], cosmological parameters were fixed and the amplitude of ISW signal was calculated from the cross-correlation data only. However, generally speaking this amplitude parameter is highly dependent on the cosmological parameters we use. Currently, the constraints on the cosmological parameters are not affected significantly by fixing the three parameters; however, this is because the present data are not very constraining. On the other hand, in our calculations we find that the constraints on bias and amplitude are different between LCDM and EDE models (see Table II and IV). This fact demonstrates that keeping these parameters fixed will lead to biased results. In other words, had we used the bias and amplitude obtained from the LCDM model to constrain the EDE model, we would have obtained different, biased results. Therefore, here we constrain all these parameters at the same time using the MCMC.

The results are shown in Table IV. The significance in sigmas is obtained by the simple calculation,  $S/N = A/\sigma_A$ . For the “UVX-All” subsample the significance of ISW is about  $2.7\sigma$ , which is consistent with other works [13, 14]. Furthermore, we also find that the low redshift subsample also gives about  $2.3\sigma$  significance, which is reduced as compared to the “All” sample due the smaller quasar number of the low redshift subsample.

The most interesting result is that the high redshift  $z > 1.5$  subsample reports a signal of ISW effect at  $\sim 1.5\sigma$  confidence level. As we know, in the pure  $\Lambda$ CDM model with the bias  $b \sim 1$ , the prediction of ISW effect should be close to zero in the high redshift  $A_{\text{amp}} \sim 0$ . However, in our analysis we obtain a higher mean value

TABLE IV. The results of amplitude of ISW signal and their significance in two dark energy models.

Subsample	Amplitude $A_{\text{amp}}$	S/N
$\Lambda$ CDM Model		
All-All	$1.51 \pm 0.73$	$2.1 \sigma$
All-Low	$3.05 \pm 1.31$	$2.3 \sigma$
All-High	$2.32 \pm 1.53$	$1.5 \sigma$
UVX-All	$2.06 \pm 0.75$	$2.7 \sigma$
UVX-Low	$4.36 \pm 1.82$	$2.4 \sigma$
UVX-High	$2.49 \pm 1.57$	$1.6 \sigma$
EDE Mocker Model		
UVX-All	$1.91 \pm 0.75$	$2.5 \sigma$
UVX-Low	$3.96 \pm 1.78$	$2.2 \sigma$
UVX-High	$2.22 \pm 1.47$	$1.5 \sigma$

and a smaller error bar. Consequently, the amplitude of ISW signal is larger than a null-detection at about  $\sim 1.5 \sigma$  confidence level. As we discussed before, this interesting non-vanishing ISW signal in the high redshift subsample may be due to the larger bias and stellar contamination at this high redshift, or some different underlying cosmological models reflecting an early departure for matter dominance in the expansion rate. The large number of quasar in the sample is also helpful in shrinking the error bar and enhancing the significance of the signal. Another intriguing result that we can appreciate from Table IV is that the discrepancies with the value  $A_{\text{amp}} = 1$ , which labels the perfect agreement between theory and data, are more severe for the lower redshift ranges than for those at high redshift. All the high-redshift samples are in fact in agreement at the  $1 \sigma$  level with the theoretical predictions either for the EDE or  $\Lambda$ CDM cosmologies. As for the low-redshift samples the discrepancies are at the  $\sim 2 \sigma$  level confirming the results of Ref. [15].

As we show in Fig. 13, at high redshift the QSO-temperature cross-correlations of the EDE model will be larger than that predicted in the  $\Lambda$ CDM framework. When combining the obtained value for the bias, the EDE model should give larger CCF values than those of  $\Lambda$ CDM model for a given cosmology. Thus, in our calculations we find that the amplitude of the ISW signal in EDE model, inversely proportional to the theoretical CCF values (see Eq. (33)), is slightly smaller than the one of  $\Lambda$ CDM model. Although other mechanisms could be in place to explain this discrepancy, either involving not properly understood systematic effects or large scale structures such as super-clusters or large voids [24], a not negligible amount of dark energy at high redshift could also help in reducing the statistical significance of this result.

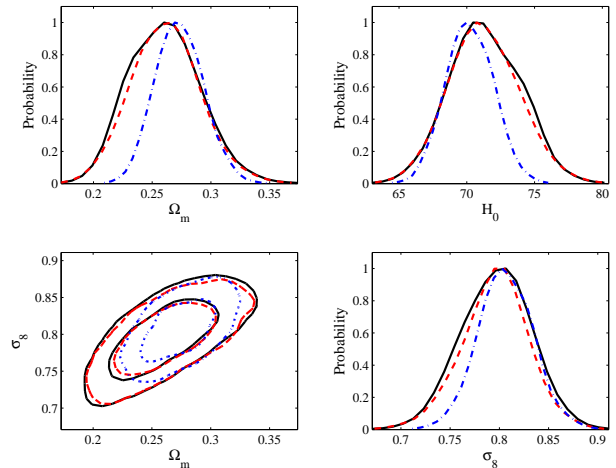


FIG. 16: Marginalized one-dimensional and two-dimensional likelihood ( $1, 2\sigma$  contours) constraints on the parameters  $\Omega_m$ ,  $H_0$  and  $\sigma_8$  in the  $\Lambda$ CDM model from different present data combinations: WMAP5 only (black solid lines), WMAP5+ISW (red dashed lines) and All datasets (blue dash-dot lines).

#### D. Cosmological Constraints

Finally we present constraints on the cosmological parameters from the ISW data, combining with the WMAP5, BAO and SNIa datasets, in two dark energy models. Here we only use the ACF and CCF data from the ‘‘UVX-All’’ subsample. The other five subsamples also give similar results. In our calculations we do not follow the previous works [13, 14] by fixing the other three parameters,  $b$ ,  $a$  and  $A_{\text{amp}}$ , to be their best fit values. In Table V we show the constraints on some related cosmological parameters from three different data combinations: WMAP5 only, WMAP5+ISW, and All datasets. And we particularly pay attention to the ISW contribution by comparing the results between WMAP5 and WMAP5+ISW.

##### 1. $\Lambda$ CDM Model

Firstly, we consider the pure  $\Lambda$ CDM model. In Fig. 16 we show the one dimensional marginalized likelihood distributions of some cosmological parameters from three data combinations. From Table V we can find that the combined constraints from WMAP5+ISW are only slightly improved over using WMAP5 only, since at present constraints from the ISW data are still very weak and in the calculations we only consider the quasar catalog and neglect other low redshift tracers which could give powerful ISW constraints [7, 14, 15]. We also show the two dimensional contour in the  $(\Omega_m, \sigma_8)$  panel. When adding the ISW data, the constraint becomes slightly

TABLE V. Constraints on the  $\Lambda$ CDM and early dark energy model from the current observations. Here we show the mean values and  $1\sigma$  error bars. For some parameters that are only weakly constrained we quote the 95% upper limit.

Parameter	WMAP5 Only	WMAP5+ISW	All Datasets
$\Lambda$ CDM Model			
$\Omega_m$	$0.261 \pm 0.030$	$0.261 \pm 0.028$	$0.273 \pm 0.019$
$\sigma_8$	$0.797 \pm 0.035$	$0.795 \pm 0.032$	$0.805 \pm 0.027$
$H_0$	$71.4 \pm 2.6$	$71.3 \pm 2.5$	$70.2 \pm 1.7$
$\Omega_{\text{EDE,sf}}$	$0.0559 \pm 0.0050$	$0.0557 \pm 0.0048$	$0.0537 \pm 0.0032$
EDE Mocker Model			
$w_0$	$< -0.694$	$< -0.708$	$< -0.909$
$C$	$< 2.950$	$< 2.623$	$< 3.214$
$\Omega_m$	$0.307 \pm 0.050$	$0.303 \pm 0.048$	$0.272 \pm 0.021$
$\sigma_8$	$0.716 \pm 0.072$	$0.714 \pm 0.070$	$0.744 \pm 0.049$
$H_0$	$66.1 \pm 4.4$	$66.3 \pm 4.3$	$69.3 \pm 1.8$
$\Omega_{\text{EDE}}(z_{\text{lss}})$	$< 0.037$	$< 0.036$	$< 0.026$
$\Omega_{\text{EDE,sf}}$	$0.0681 \pm 0.0144$	$0.0682 \pm 0.0139$	$0.0644 \pm 0.0104$

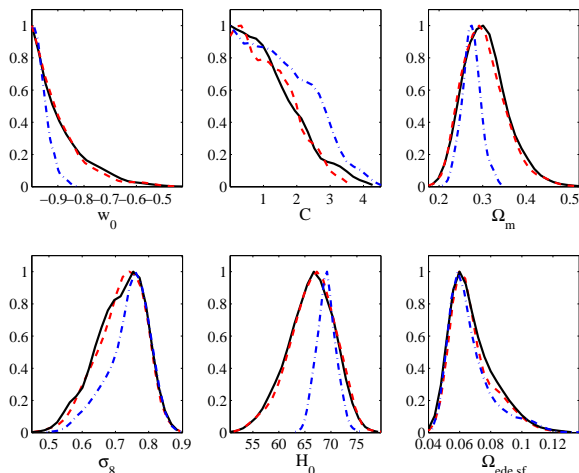


FIG. 17: One-dimensional marginalized likelihood constraints on the dark energy parameters  $w_0$  and  $C$ , as well as  $\Omega_m$ ,  $H_0$ ,  $\sigma_8$  and  $\Omega_{\text{EDE,sf}}$  from different present data combinations: WMAP5 only (black solid lines), WMAP5+ISW (red dashed lines) and All datasets (blue dash-dot lines).

more stringent.

When combining all the datasets together, the constraints tighten significantly: the error bars of some parameters are reduced by a factor of 1.5. These are due to the constraining power of SNIa and BAO. These results are consistent with some previous works [1, 88] and also with the recent findings based on the clustering of luminous red galaxies of the DR7 [89]. Thus, present data sets allow to constrain the amount of dark energy in the structure formation era at the percent level.

## 2. EDE Mocker Model

Due to the lack of cosmological probes, the behaviour of the dark energy component is very poorly constrained in the redshift range  $2 < z < 1100$ . Therefore, when using WMAP5 data only, the constraints on the parameters  $w_0$  and  $C$ , describing the equation of state of early dark energy, are very weak, namely the 95% upper limits are  $w_0 < -0.694$  and  $C < 2.950$ . Consequently, current observations still allow very large amount of early dark energy at high redshift  $z \sim 1090$  as  $\Omega_{\text{EDE}}(z_{\text{lss}}) < 0.037$  (95% C.L.), which is consistent with the results obtained by Refs. [41, 54, 90]. Early dark energy models with a non-negligible fraction of dark energy density still fit the CMB data very well.

When comparing the results of  $\Lambda$ CDM and EDE model, the error bars of some parameters are significantly enlarged by a factor of two, shown in Fig.17, due to the degeneracies between the dark energy parameters and other background parameters. We find that the constraint on the parameter  $\Omega_{\text{EDE,sf}}$  becomes rather weak for EDE. The current constraint on  $\Omega_{\text{EDE,sf}}$  is  $\Omega_{\text{EDE,sf}} = 0.0681 \pm 0.0144$  at  $1\sigma$  confidence level, which is obviously higher than the pure  $\Lambda$ CDM model, although the two agree at  $1\sigma$  level:  $\Omega_{\text{EDE,sf}} = 0.0559 \pm 0.0050$  ( $1\sigma$ ). This is because of the higher dark energy abundance at high redshifts with respect to  $\Lambda$ CDM. Moreover, the linear growth factor of early dark energy model is suppressed significantly by the large value of parameter  $C$ . When the fraction of dark energy density becomes large in the EDE model, the present value of  $\sigma_8$  will be lower,  $\sigma_8 = 0.716 \pm 0.072$  ( $1\sigma$ ), which is obviously lower than one obtained in the pure  $\Lambda$ CDM framework:  $\sigma_8 = 0.797 \pm 0.035$  ( $1\sigma$ ), while the error bar is enlarged by a factor of two [41]. In Fig. 18 we can clearly see the anti-correlation between  $\sigma_8$  and  $\Omega_{\text{EDE,sf}}$ .

Although the ISW data are directly related to the dark

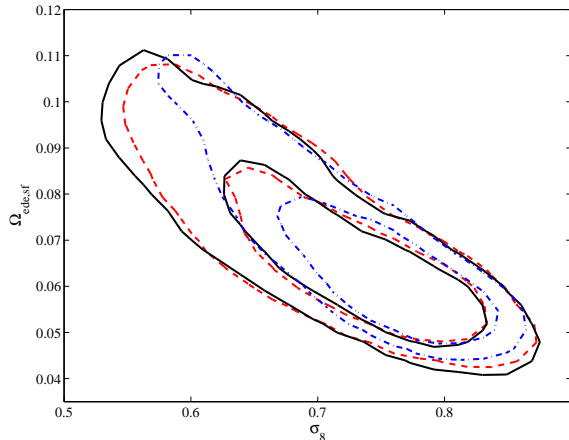


FIG. 18: Two dimensional contour in the  $(\sigma_8, \Omega_{\text{EDE},\text{sf}})$  panel from different present data combinations: WMAP5 only (black solid lines), WMAP5+ISW (red dashed lines) and All datasets (blue dash-dot lines).

energy parameters and contain information on the low redshift universe ( $z < 5$ ), at present the constraints are too weak to offer much improvement. In fact, the results do not improve significantly when adding the ISW data, which is shown in Fig. 20 and Table V. The constraints on  $w_0$  and  $C$  improve slightly:  $w_0 < -0.708$  and  $C < 2.623$  at 95% confidence level which are close to the pure  $\Lambda$ CDM model. Meanwhile, the constraints on other cosmological parameters, such as  $\sigma_8$  and  $\Omega_{\text{EDE},\text{sf}}$ , also tighten a little, but not significantly. In Fig. 18 we plot the two dimensional constraint on  $(\sigma_8, \Omega_{\text{EDE},\text{sf}})$  from different data combinations. WMAP5+ISW data combination gives clearly tighter constraints than WMAP5 only.

Finally, we add some low-redshift observational data, such as SNIa and BAO data. Due to their constraining power, the constraint on  $w_0$  improves significantly:  $w_0 < -0.909$  at 95% confidence level. However, the 95% upper limit on  $C$  has not been improved:  $C < 3.214$ , because of the anti-correlation between  $w_0$  and  $C$  [41]. The constraints on other parameters, when combining all datasets together, become slightly more stringent and are consistent with the previous work [41], in which a similar analysis was carried using gamma-ray bursts and Lyman- $\alpha$  forest observations instead of the ISW effect.

### VIII. FUTURE RESULTS

From the results presented above, we see that both in  $\Lambda$ CDM and EDE model, the ISW data give a little improvement on the constraints on the cosmological parameter we considered, when compared to other observations, such as SNIa and BAO. Therefore, it is worthwhile discussing whether future ISW data could give more strin-

TABLE VI. Constraints on the  $\Lambda$ CDM model from the future measurements. Here we show the standard deviations.

Parameter	CMB	CMB+ISW	All Datasets
$\Lambda$ CDM Model			
$b$	—	—	0.1943
$a$	—	—	0.0016
$A_{\text{amp}}$	—	—	0.2856
$\Omega_{\text{m}}$	0.0090	0.0080	0.0029
$\sigma_8$	0.0075	0.0070	0.0054
$H_0$	0.7730	0.7012	0.2327
$\Omega_{\text{EDE},\text{sf}}$	0.0014	0.0013	0.0005

gent constraints on the cosmological parameters. For this purpose we have performed a further analysis and we have chosen two fiducial models in perfect agreement with current data: a pure  $\Lambda$ CDM model and an EDE model with parameters taken to be the best-fit values from the current constraints of “All” datasets combination.

#### A. $\Lambda$ CDM Model

Firstly, we use the fiducial  $\Lambda$ CDM mock datasets to constrain the parameters in the  $\Lambda$ CDM model, as well as other three parameters,  $b$ ,  $a$  and  $A_{\text{amp}}$ . In Table VI we list the standard deviations of those parameters from these mock future measurements. We remind that the mock ISW data sets consist of data with covariance matrix reduced by a factor nine when compared to the present ACF and CCF data.

Due to the smaller error bars of the mock data sets, the constraints on the cosmological parameters from CMB only improve significantly by a factor of three, when comparing to the current results. When adding the simulated ISW data, the constraints improve further and the improvements are larger than those from the current observations, since the ISW data with smaller error bars are now more helpful in breaking the degeneracies between the parameters that keep the CMB angular diameter distance unchanged.

When using all datasets together, we present the constraints on the cosmological parameters, as well as those of three parameters. The constraints on the parameters improve significantly. In particular, due to the more accurate ISW data, the standard deviations of  $b$ ,  $a$  and  $A_{\text{amp}}$  have been shrunk to 0.19, 0.15% and 0.29. In this case, the significance of ISW signal will be clearly enhanced. The future CMB measurement and galaxy survey could be very useful to detect the ISW effect at a much higher significance than now and also to constrain the bias at high redshift.

TABLE VII. Constraints on the early dark energy model from the future measurements. Here we show the standard deviations. For some parameters that are only weakly constrained we quote the 95% upper limit.

Parameter	CMB	CMB+ISW	All Datasets	CMB	CMB+ISW	All Datasets
	Fiducial $\Lambda$ CDM Model			Fiducial EDE Mocker Model		
$w_0$	$< -0.4952$	$< -0.6586$	$< -0.9571$	$< -0.6154$	$< -0.6455$	$< -0.9041$
$C$	$< 1.4452$	$< 1.8473$	$< 2.7632$	$< 3.3496$	$< 1.9581$	$< 2.4893$
$\Omega_m$	0.0642	0.0412	0.0031	0.0494	0.0406	0.0033
$\sigma_8$	0.0607	0.0425	0.0108	0.0512	0.0433	0.0188
$H_0$	5.3335	3.7914	0.3186	5.0357	3.8344	0.4733
$\Omega_{\text{EDE}}(z_{\text{ISS}})$	$< 0.0063$	$< 0.0057$	$< 0.0035$	$< 0.0141$	$< 0.0129$	$< 0.0122$
$\Omega_{\text{EDE,sf}}$	0.0055	0.0039	0.0018	0.0060	0.0054	0.0043

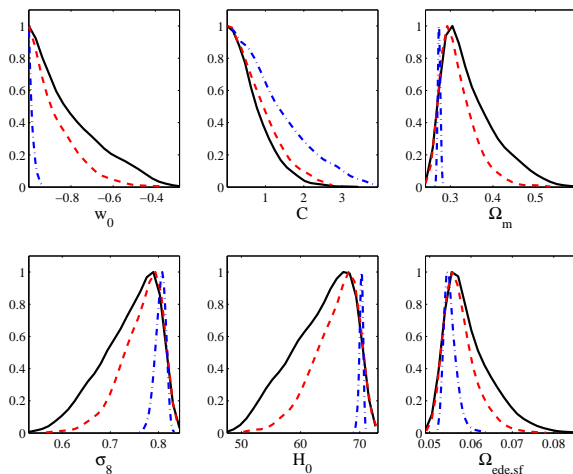


FIG. 19: One dimensional marginalized likelihood constraints on the dark energy parameters  $w_0$  and  $C$ , as well as  $\Omega_m$ ,  $H_0$ ,  $\sigma_8$  and  $\Omega_{\text{EDE,sf}}$  from different mock futuristic data combinations with the fiducial  $\Lambda$ CDM model: CMB only (black solid lines), CMB+ISW (red dashed lines) and All datasets (blue dash-dot lines).

## B. EDE Mocker Model

### 1. Fiducial $\Lambda$ CDM

Firstly, we choose the pure  $\Lambda$ CDM as the fiducial model. In table VII we list the forecasts for some related parameters using the future measurements.

From Fig. 19 and Table VII, we can find that the CMB data only cannot constrain the cosmological parameters well, as we expect. In fact, the standard deviations of parameters are rather large. Early dark energy models with a non-negligible fraction of dark energy density cannot be ruled out by the CMB data only, namely the constraint on the fraction of dark energy density at  $z \sim 1090$  is  $\Omega_{\text{EDE}}(z_{\text{ISS}}) < 0.0063$  (95% C.L.).

Interestingly, when including the future ISW data,

the constraints on the parameters improve significantly, unlike for the current results. The 95% upper limit of current equation of state of dark energy  $w_0$  is now  $w_0 < -0.659$ , while  $w_0 < -0.495$  (95% C.L.) obtained from CMB data only. By contrast, the constraint on  $C$  has not been improved significantly:  $C < 1.847$  (95% C.L.), due to the anti-correlation between  $w_0$  and  $C$ . Meanwhile, all of the related parameters have been constrained more tightly than ones from CMB data only by a factor of two. This simulated ISW data with smaller error bars is effective in breaking the degeneracies among the parameters.

Furthermore, when using all datasets, from Fig. 19 and Table VII we can find that the constraints of many parameters have been tightened significantly and the degeneracies have been broken further. The constraint on  $w_0$  becomes very tight  $w_0 < -0.957$  at 95% confidence level, due to the accurate Supernovae data. And since the 95% upper limit of  $\Omega_{\text{EDE}}(z_{\text{ISS}})$  is also suppressed apparently,  $\Omega_{\text{EDE}}(z_{\text{ISS}}) < 0.0035$ , many early dark energy models can be ruled out.

### 2. Fiducial EDE

We also choose the EDE fiducial model to determine the cosmological parameters. The one-dimensional constraints of some related parameters from different data combinations are plotted in Fig. 20. We obtain similar conclusions to the  $\Lambda$ CDM case.

The CMB data only cannot constrain the parameters very well. When including the ISW data, the constraints on the parameters improve significantly. However, even using CMB+ISW data combination, the best fit values of  $w_0$  and  $C$  are still close to the  $\Lambda$ CDM model. In this case, early dark energy models cannot be distinguished from the pure  $\Lambda$ CDM model.

Finally, the ‘‘All’’ datasets combination give the most stringent constraints on the parameters. In this case, the peaks of one dimensional distributions of  $w_0$  and  $C$  are moving away from the  $\Lambda$ CDM model,  $w_0 = -1$ ,  $C = 0$ , see Fig. 20. The 95% confidence level are  $w_0 < -0.904$  and  $C < 2.489$ , respectively. These results imply that

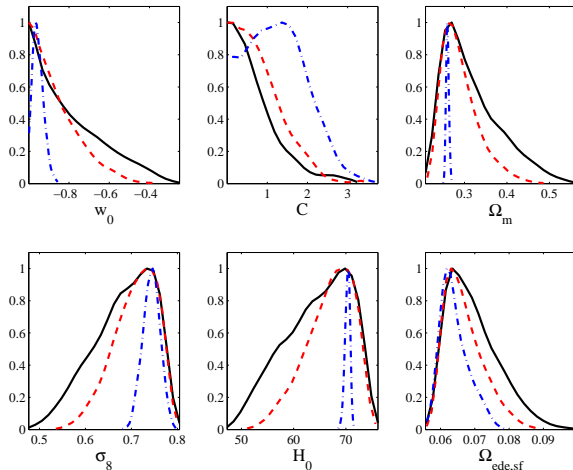


FIG. 20: One dimensional constraints on the dark energy parameters  $w_0$  and  $C$ , as well as  $\Omega_m$ ,  $H_0$ ,  $\sigma_8$  and  $\Omega_{\text{EDE},\text{sf}}$  from different mock futuristic data combinations with the fiducial EDE model: CMB only (black solid lines), CMB+ISW (red dashed lines) and All datasets (blue dash-dot lines).

the future measurements could distinguish between the pure  $\Lambda$ CDM model and early dark energy models.

## IX. CONCLUSIONS AND DISCUSSIONS

Most cosmological probes are sensitive to the behaviour of dark energy at very low redshift; thus, it is of great interest to investigate those observable which are able to complement the analysis with constraints on the dark energy abundance at high redshifts, close to the onset of cosmic acceleration and possibly to the regime which is probed by other large scale structure observables like the Lyman- $\alpha$  forest [91]. In this paper we exploited the capabilities of the ISW effect in the high redshift universe, using the cross-correlation signal between the one million photometrically selected QSOs of the SDSS DR6 catalog [45] and the CMB maps of the WMAP year 5 satellite [51]. From the SDSS DR6-QSO catalog we extract the QSO ACF and estimate the bias and stellar contamination by considering several redshift ranges between  $z = 0$  and  $z = 5$ . We have given particular emphasis to our subsamples at  $z > 1.5$  where an overall weak evidence for a non-zero ISW signal is found at the  $1.5\sigma$  confidence level. The evidence is instead at the  $2.7\sigma$  level if we consider the whole sample and this is in agreement with investigations based on similar samples [14, 15]. Our high-redshift sample has a mean redshift of  $z = 2$  and  $z = 2.3$  if we choose the conservative QSO sample or the speculative one (sources with no ultra-violet excess), respectively. This is a new regime when compared to other probes that have been more extensively used for ISW studies such as galaxies or X-ray

observations.

We have focused on modifications to the standard  $\Lambda$ CDM cosmology that results in a non-negligible amount of dark energy in the structure formation era: these models are generically labeled as Early Dark Energy models and are characterized by an early departure for matter dominance in the cosmic expansion, with consequences for background evolution and therefore structure formation. We found that at present the results are still rather weak to provide competitive constraints on the parameters describing either the  $\Lambda$ CDM or EDE models, even though constraints at the percent of sub-percent level on the energy density contribution of this component in the structure formation era can be achieved. Adding present high redshift ISW data to CMB data from WMAP does not improve the constraints significantly. However, we also forecast future performance of QSO data by assuming a measurements of CCF and ACF data by reducing the error bars by a factor three and combining these with mock Planck data. In this case the results are particularly interesting since the improvement to CMB data alone when adding the ISW information can result in a factor 1.5 on most of the cosmological parameters. If we further add some Supernovae luminosity distance moduli like those that can be provided by the SNAP satellite the constraints can become even tighter and up to a factor between 3-10 better than the CMB alone.

Here we summarize our main conclusions in more detail:

- We compute the QSO Auto-Correlation Function (ACF) from SDSS DR6-QSO and extract bias and catalog efficiency: we measure the quasar-matter bias and the typical error on the bias is at the level of  $\sigma_b = 0.8$  when we split in five bins the sample and of  $\sigma_b = 0.3$  when we consider the whole sample. We present results for a more conservative selection of QSOs using also ultra-violet excess flags and a less conservative selection that consider all the sources of the catalog.
- EDE models usually result in higher values for the bias than those of  $\Lambda$ CDM by  $\sim 10\%$ , due to the slower growth of density perturbations in EDE cosmology that requires a higher bias to match the observed value.
- We compute CCF values by cross-correlating the QSO number density with the CMB temperature and found an evidence at  $2.7\sigma$  level for the all sample for an ISW effect. At high redshift this evidence reduces to  $1.5\sigma$ , which interestingly compares with the prediction of null detection in  $\Lambda$ CDM. This non-vanishing signal could be caused by the large bias, stellar contamination and large number of quasar sample, or an higher dark energy abundance at high redshifts. However, at present this signal is still too weak to distinguish between the  $\Lambda$ CDM and early dark energy models.

- The parameter  $A_{\text{amp}}$  was used to quantify the disagreement between theoretical predictions and data. We found that this disagreement vanishes in the high redshift subsample, either for EDE or  $\Lambda$ CDM models and is instead at the  $\sim 2\sigma$  level for the low-redshift subsamples.
- We forecasted futuristic large-scale structure measurement of the ISW effect using the cross-correlation that can be provided by photometric surveys. Assuming smaller error bars by a factor of three, the more accurate ISW data is helpful to break the degeneracies among some parameters and results in an overall improvement on mock Planck data alone by a factor 1.5. Furthermore, the standard derivations of those three parameters,  $b$ ,  $a$  and  $A_{\text{amp}}$ , are also shrunk significantly. The future CMB measurement and galaxy survey could be very useful to detect the ISW effect at a much higher significance.
- Further adding Supernovae measurements improve results by a factor 3-10 due to the better determination of  $H_0$  and  $\Omega_m$  that can be provided by SNAP observations.

The use of this state-of-the-art QSO catalogue can open up a completely new window on the high-redshift large scale structure of the universe and allowing for a

quantitative use of the ISW effect in a regime  $z > 1.5$ , which is at present weakly probed by observations. Either a confirmation of the  $\Lambda$ CDM model or possible departures induced by modified gravity or quintessence could be of fundamental importance and will be addressed by the surveys of the near future.

### Acknowledgments

The numerical analysis has been performed on the COSMOS supercomputer at DAMTP and on Darwin Supercomputer of the University of Cambridge High Performance Computing Service (<http://www.hpc.cam.ac.uk/>), provided by Dell Inc. using Strategic Research Infrastructure Funding from the Higher Education Funding Council for England. Some of the results in this paper have been derived using the HEALPix package [48]. We thank G. De Zotti, T. Giannantonio, A. Myers, C. Morossi, A. Raccanelli, and G. Richards for useful discussions. We also thank the referee for the very helpful report. This research has been partially supported by ASI Contract No. I/016/07/0 COFIS and the INFN-PD51 grant. MV thanks the Institute of Astronomy in Cambridge (UK) for hospitality when part of this work was done.

- 
- [1] E. Komatsu *et al.*, *Astrophys. J. Suppl.* **180**, 330 (2009).  
 [2] M. Kowalski *et al.*, *Astrophys. J.* **686**, 749 (2008).  
 [3] E. J. Copeland, M. Sami and S. Tsujikawa, *Int. J. Mod. Phys. D* **15**, 1753 (2006).  
 [4] R. K. Sachs and A. M. Wolfe, *Astrophys. J.* **147**, 73 (1967).  
 [5] R. G. Crittenden and N. G. Turok, *Phys. Rev. Lett.* **76**, 575 (1996).  
 [6] S. P. Boughn, R. G. Crittenden, and N. G. Turok, *New Astron.* **3**, 275 (1998).  
 [7] A. Raccanelli *et al.*, *Mon. Not. Roy. Astron. Soc.* **386**, 2161 (2008).  
 [8] M. R. Nolta *et al.*, *Astrophys. J.* **608**, 10 (2004).  
 [9] N. Afshordi, Y. S. Loh, and M. A. Strauss, *Phys. Rev. D* **69**, 083524 (2004).  
 [10] A. Rassat, K. Land, O. Lahav, and F. B. Abdalla, *Mon. Not. Roy. Astron. Soc.* **377**, 1085 (2007).  
 [11] A. Cabré, E. Gaztañaga, M. Manera, P. Fosalba, and F. Castander, *Mon. Not. Roy. Astron. Soc.* **372**, L23 (2006).  
 [12] A. Cabré, P. Fosalba, E. Gaztañaga, and M. Manera, *Mon. Not. Roy. Astron. Soc.* **381**, 1347 (2007).  
 [13] T. Giannantonio *et al.*, *Phys. Rev. D* **74**, 063520 (2006).  
 [14] T. Giannantonio *et al.*, *Phys. Rev. D* **77**, 123520 (2008).  
 [15] S. Ho, C. Hirata, N. Padmanabhan, U. Seljak, and N. Bahcall, *Phys. Rev. D* **78**, 043519 (2008).  
 [16] C. Hirata, S. Ho, N. Padmanabhan, U. Seljak, and N. Bahcall, *Phys. Rev. D* **78**, 043520 (2008).  
 [17] D. J. Schlegel *et al.*, in *Bulletin of the American Astronomical Society* (2007), vol. 38 of *Bulletin of the American Astronomical Society*, pp. 966+.  
 [18] D. J. Schlegel *et al.*, arXiv:0904.0468.  
 [19] A. Vallinotto, S. Das, D. N. Spergel, and M. Viel, arXiv:0903.4171.  
 [20] M. Frommert, T. A. Enßlin, and F. S. Kitaura, *Mon. Not. Roy. Astron. Soc.* **391**, 1315 (2008).  
 [21] A. Rassat, arXiv:0902.1759.  
 [22] Y. C. Cai, S. Cole, A. Jenkins, and C. Frenk, *Mon. Not. Roy. Astron. Soc.* **396**, 772 (2009).  
 [23] B. M. Schaefer, M. Douspis, and N. Aghanim, arXiv:0903.4288.  
 [24] B. R. Granett, M. C. Neyrinck, and I. Szapudi, *Astrophys. J.* **683**, L99 (2008).  
 [25] J. Lesgourgues, W. Valkenburg, E. Gaztañaga, *Phys. Rev. D*, **77**, 063505 (2008).  
 [26] L. Pogosian, P.S. Corasaniti, C. Stephan-Otto, R. Crittenden, R. Nichol, *Phys. Rev. D.*, **72**, 103519, (2005).  
 [27] U. Seljak *et al.*, *Phys. Rev. D* **71**, 103515 (2005).  
 [28] M. Doran, J. M. Schwindt and C. Wetterich, *Phys. Rev. D* **64**, 123520 (2001).  
 [29] E. V. Linder and A. Jenkins, *Mon. Not. Roy. Astron. Soc.* **346**, 573 (2003).  
 [30] K. Dolag, M. Bartelmann, F. Perrotta, C. Baccigalupi, L. Moscardini, M. Meneghetti and G. Tormen, *Astron. Astrophys.* **416**, 853 (2004).  
 [31] R. Mainini, A. V. Maccio, S. A. Bonometto and A. Klypin, *Astrophys. J.* **599**, 24 (2003).  
 [32] D. Crociani, M. Viel, L. Moscardini, M. Bartelmann and

- M. Meneghetti, *Mon. Not. Roy. Astron. Soc.* **385**, 728 (2008).
- [33] M. Bartelmann, M. Doran and C. Wetterich, *Astron. Astrophys.* **454**, 27 (2006).
- [34] C. Fedeli and M. Bartelmann, *Astron. Astrophys.* **461**, 49 (2007).
- [35] V. Acquaviva and C. Baccigalupi, *Phys. Rev. D* **74**, 103510 (2006).
- [36] K. M. Smith, W. Hu and M. Kaplinghat, *Phys. Rev. D* **74**, 123002 (2006).
- [37] M. Manera and D. F. Mota, *Mon. Not. Roy. Astron. Soc.* **371**, 1373 (2006).
- [38] M. J. Francis, G. F. Lewis and E. V. Linder, *Mon. Not. Roy. Astron. Soc. Lett.* **393**, L31 (2008).
- [39] D. F. Mota, *JCAP* **0809**, 006 (2008).
- [40] M. Grossi and V. Springel, arXiv:0809.3404.
- [41] J. Q. Xia and M. Viel, *JCAP* **0904**, 002 (2009).
- [42] L. Hollenstein, D. Sapone, R. Crittenden, and B. M. Schäfer, *JCAP* **0904**, 012 (2009).
- [43] H. V. Peiris and D. N. Spergel, *Astrophys. J.* **540**, 605 (2000).
- [44] A. Cooray, *Phys. Rev. D* **65**, 103510 (2002).
- [45] G. T. Richards *et al.*, *Astrophys. J. Suppl.* **180**, 67 (2009).
- [46] G. T. Richards *et al.*, *Astrophys. J. Suppl.* **155**, 257 (2004).
- [47] A. D. Myers *et al.*, *Astrophys. J.* **638**, 622 (2006).
- [48] Górski *et al.*, *Astrophys. J.* **622**, 759 (2005).
- [49] S. D. Landy and A. S. Szalay, *Astrophys. J.* **412**, 64 (1993).
- [50] R. Scranton *et al.*, *Astrophys. J.* **579**, 48 (2002).
- [51] G. Hinshaw *et al.*, *Astrophys. J. Suppl.* **180**, 225 (2009); URL: <http://lambda.gsfc.nasa.gov/>.
- [52] B. Gold *et al.*, *Astrophys. J. Suppl.* **180**, 265 (2009).
- [53] C. Wetterich, *Phys. Lett. B* **594**, 17 (2004).
- [54] E. V. Linder, *Astropart. Phys.* **26**, 16 (2006).
- [55] A. Lewis, A. Challinor, and A. Lasenby, *Astrophys. J.* **538**, 473 (2000); URL: <http://camb.info/>.
- [56] J. Dunkley *et al.*, *Astrophys. J. Suppl.* **180**, 306 (2009).
- [57] E. L. Wright *et al.*, *Astrophys. J. Suppl.* **180**, 283 (2009).
- [58] M. R. Nolta *et al.*, *Astrophys. J. Suppl.* **180**, 296 (2009).
- [59] D. J. Eisenstein *et al.* *Astrophys. J.* **633**, 560 (2005).
- [60] S. Cole *et al.* *Mon. Not. Roy. Astron. Soc.* **362**, 505 (2005).
- [61] G. Huetsi, *Astron. Astrophys.* **449**, 891 (2006).
- [62] W. J. Percival *et al.*, *Mon. Not. Roy. Astron. Soc.* **381**, 1053 (2007).
- [63] A. Albrecht *et al.*, arXiv:astro-ph/0609591.
- [64] T. Okumura, T. Matsubara, D. J. Eisenstein, I. Kayo, C. Hikage, A. S. Szalay and D. P. Schneider, *Astrophys. J.* **677**, 889 (2008).
- [65] D. J. Eisenstein and W. Hu, *Astrophys. J.* **496**, 605 (1998).
- [66] E. Di Pietro and J. F. Claeskens, *Mon. Not. Roy. Astron. Soc.* **341**, 1299 (2003).
- [67] W. L. Freedman *et al.*, *Astrophys. J.* **553**, 47 (2001).
- [68] Planck Collaboration, arXiv:astro-ph/0604069.
- [69] J. Q. Xia, H. Li, G. B. Zhao and X. Zhang, *Int. J. Mod. Phys. D* **17**, 2025 (2008).
- [70] A. G. Kim, E. V. Linder, R. Miquel and N. Mostek, *Mon. Not. Roy. Astron. Soc.* **347**, 909 (2004).
- [71] J. A. Tyson, in Proc. SPIE 4836, *Survey and Other Telescope Technologies and Discoveries*, ed. J. A. Tyson and S. Wolff (Bellingham, WA: SPIE) (2002).
- [72] N. Kaiser *et al.*, in Proc. SPIE 4836, *Survey and Other Telescope Technologies and Discoveries*, ed. J. A. Tyson and S. Wolff (Bellingham, WA: SPIE) (2002).
- [73] A. Lewis and S. Bridle, *Phys. Rev. D* **66**, 103511 (2002); URL: <http://cosmologist.info/cosmomc/>.
- [74] J. Weller and A. M. Lewis, *Mon. Not. Roy. Astron. Soc.* **346**, 987 (2003).
- [75] G. B. Zhao, J. Q. Xia, M. Li, B. Feng and X. Zhang, *Phys. Rev. D* **72**, 123515 (2005).
- [76] J. Q. Xia, G. B. Zhao, B. Feng, H. Li and X. Zhang, *Phys. Rev. D* **73**, 063521 (2006).
- [77] P. S. Corasaniti, T. Giannantonio and A. Melchiorri, *Phys. Rev. D* **71**, 123521 (2005).
- [78] D. Pietrobon, A. Balbi and D. Marinucci, *Phys. Rev. D* **74**, 043524 (2006).
- [79] S. M. Croom *et al.*, *Mon. Not. Roy. Astron. Soc.* **349**, 1397 (2004).
- [80] A. D. Myers *et al.*, *Astrophys. J.* **658**, 85 (2007).
- [81] S. Matarrese, P. Coles, F. Lucchin and L. Moscardini, *Mon. Not. Roy. Astron. Soc.* **286**, 115 (1997).
- [82] L. Moscardini, P. Coles, F. Lucchin and S. Matarrese, *Mon. Not. Roy. Astron. Soc.* **299**, 95 (1998).
- [83] P. Martini and D. H. Weinberg, *Astrophys. J.* **547**, 12 (2001).
- [84] C. Porciani, M. Magliocchetti and P. Norberg, *Mon. Not. Roy. Astron. Soc.* **355**, 1010 (2004).
- [85] A. M. Weinstein *et al.*, *Astrophys. J. Suppl.* **155**, 243 (2004).
- [86] S. M. Croom *et al.*, *Mon. Not. Roy. Astron. Soc.* **356**, 415 (2005).
- [87] Y. Shen *et al.*, *Astron. J.* **133**, 2222 (2007).
- [88] J. Q. Xia, H. Li, G. B. Zhao and X. Zhang, *Phys. Rev. D* **78**, 083524 (2008).
- [89] B. A. Reid *et al.*, arXiv:0907.1659.
- [90] W. Lee and K. W. Ng, *Phys. Rev. D* **67**, 107302 (2003).
- [91] M. Viel, S. Matarrese, T. Theuns, D. Munshi, Y. Wang, *Mon. Not. Roy. Astron. Soc.* **340**, 47 (2003).